

Inherited Crustal Features and Southern Alaska Tectonic History Constrained by Sp Receiver Functions

Michael Everett Mann¹, Karen M Fischer¹, and Jeff Apple Benowitz²

¹Department of Earth, Environmental and Planetary Sciences, Brown University

²GeoSep Services

February 28, 2024

1 Inherited Crustal Features and Southern Alaska Tectonic History Constrained by Sp Receiver
2 Functions
3

4 Michael Everett Mann¹, Karen M. Fischer¹, Jeff Apple Benowitz²
5

6 ¹ Department of Earth, Environmental and Planetary Sciences, Brown University, Providence,
7 RI, USA

8 ² GeoSep Services, 1521 Pine Cone Road, Moscow, ID, USA

9 Corresponding author: Michael Everett Mann (michael_mann@brown.edu)
10
11

12 **Abstract**

13 Southern Alaska is a collage of fault-bounded accreted terranes. The deformation history
14 of these crustal blocks and geometric history of the bounding faults reflect both inherited features
15 and subsequent convergent margin events. Multiple dense (<20-km spacing) arrays of broadband
16 seismometers across southern Alaska has previously allowed for imaging of crustal structure
17 across the region using various seismic imaging methods. Here, we employ S-to-P receiver
18 functions to investigate the crustal structure of southern Alaska for signals of dynamic tectonic
19 activity. The subduction zone plate interface and subducting slab Moho are imaged dipping at
20 shallow (<60-km) depths across the southernmost part of the subduction zone. Along two
21 different transects, an inboard-dipping (~15°) boundary is imaged intersecting the trace of the
22 Border Ranges Fault at the surface that we infer represents an unrotated inboard-dipping paleo-
23 subduction (Mesozoic) interface. This observation is combined with previous seismic imaging
24 along both the Border Ranges Fault and the next seaward terrane-bounding fault—the Contact
25 Fault—to buttress a known history of convergent tectonics that varies along the margin. Along
26 with large (>10-km) crustal thickness offsets imaged across both the Denali Fault system and the

27 Eureka Creek Fault, this feature supports a Mesozoic-to-Present inboard-dipping (east and
28 northward) subduction polarity in the region. Additionally, the Sp CCP volume reveals a 100-km
29 x 50-km sized positive velocity gradient with depth (PVG) at ~25-km depth beneath the Copper
30 River Basin, which we interpret as the top of a region of active underplating and/or intrusion of
31 basaltic magmatism into the lower crust. This feature may be related to the generation of a new
32 Wrangell Volcanic Field volcano, resulting from the underlying tear in the subducting slab.

33 **1. Introduction**

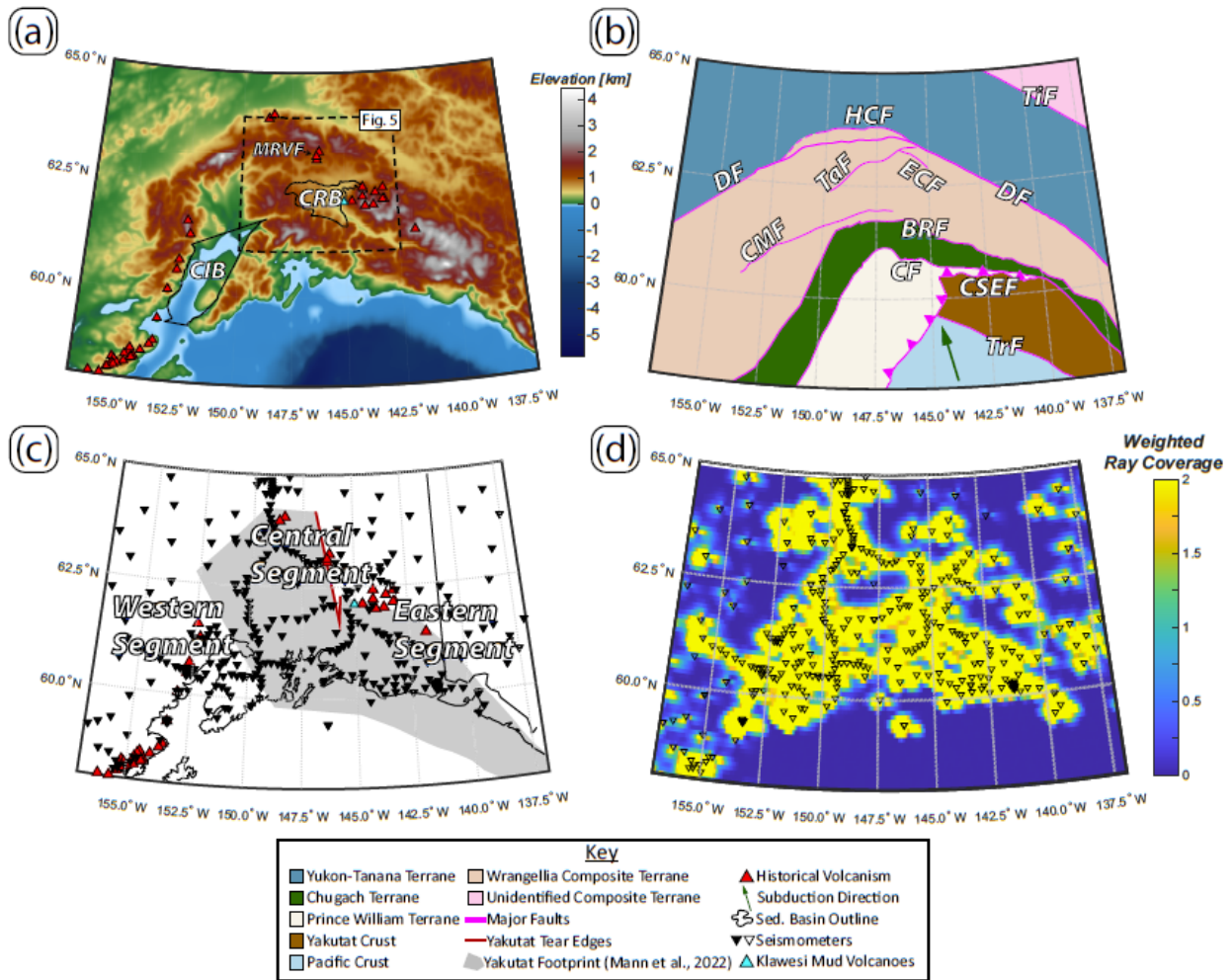
34 Continental crust is a palimpsest of tectonic activity, where ancient terrane boundaries
35 and convergent margin structures can persist for 10's of millions of years (e.g., Korja &
36 Heikkinen, 2008; Hopper et al., 2017; Long et al., 2019; Li et al., 2020). Thus, imaging crustal
37 architecture can help piece together the inherited and deformation history of a region (e.g., Fuis
38 et al., 2008; Korja & Heikkinen, 2008). Southern Alaska has been a convergent margin since at
39 least the Jurassic, leading to a tectonic quilt of Mezo-Cenozoic tectonostratigraphic accreted
40 terranes (e.g., Nokleberg et al., 1985; Plafker & Berg, 1994). Furthermore, because of successive
41 periods of crustal-scale strike-slip faulting parallel to the western North America margin and
42 dissecting southern Alaska, these accreted terranes have been transported large distances (>1000
43 km) along the margin of western North America through time (e.g., Tikoff et al., 2023). Hence
44 the region is a prime location to investigate inherited versus developed tectonic features, how
45 structural architecture can be preserved through subsequent accretion events, and how these
46 processes are expressed in seismic velocity structure.

47 Teleseismic scattered-wave imaging has been used for decades to investigate the crustal
48 structure of southern Alaska (e.g., Ferris et al., 2003; Rondenay et al., 2008; Kim et al., 2014;

49 Miller et al., 2018; Zhang et al., 2019; Mann et al., 2022; Gama et al., 2022a). Body waves
50 incident on velocity gradients, such as the Moho, generate scattered waves which can be
51 extracted from within the P-coda (for incident P waves) or preceding the S-wave arrival (for
52 incident S waves) through deconvolution, resulting in receiver functions (RFs; e.g., Langston,
53 1977; Farra & Vinnik, 2000). Analysis of these S-to-P scattered phases as measured in RFs (i.e.,
54 Sp RFs) has often been aimed at subhorizontal Moho and lithospheric discontinuities (e.g., Lekić
55 et al., 2011; Gama et al., 2022a), although Sp RFs have also been used to image dipping modern
56 and paleo structural features, for example in subduction zones (e.g., Kawakatsu et al., 2009;
57 Kumar & Kawakatsu, 2011).

58 For this study, a recently developed Sp RF common-conversion point (CCP) stacking
59 imaging procedure (Hua et al., 2020a) was applied to teleseismic S-waves recorded on dense
60 seismometer arrays across southern Alaska (Figure 1). This Sp CCP volume reveals inboard-
61 dipping features extending to depth from the surface trace of the Border Ranges Fault system
62 (BRF) that potentially are associated with the Mesozoic paleo-subduction zone when a
63 subduction interface was located along the BRF (e.g., Trop and Ridgway, 2007). We integrate
64 our new results with previous seismic imaging work on the BRF and Contact Fault (e.g.,
65 Stephens et al., 1990; Fuis et al., 1991; Ye et al., 1997) to investigate along-strike variations in
66 paleo-subduction interface preservation and modification (e.g., its rotation towards vertical dip),
67 as well as linked contractional histories. Sharp Moho offsets across terrane-bounding faults
68 including the Denali Fault and Eureka Creek Fault are also imaged. Additionally, the Sp CCP
69 volume reveals a 100-km x 50-km sized positive velocity gradient with depth (PVG) at ~25-km
70 depth beneath the Copper River Basin. Combined with recent seismic analyses across the region,

71 this mid-crustal discontinuity coincides with a dense cluster of earthquakes and may represent
 72 active underplating and/or intrusion of basaltic magmatism into the lower crust, rising from a
 73 tear in the subducting Yakutat slab which is located directly beneath this discontinuity (Mann et
 74 al., 2022; Brueseke et al., 2023).

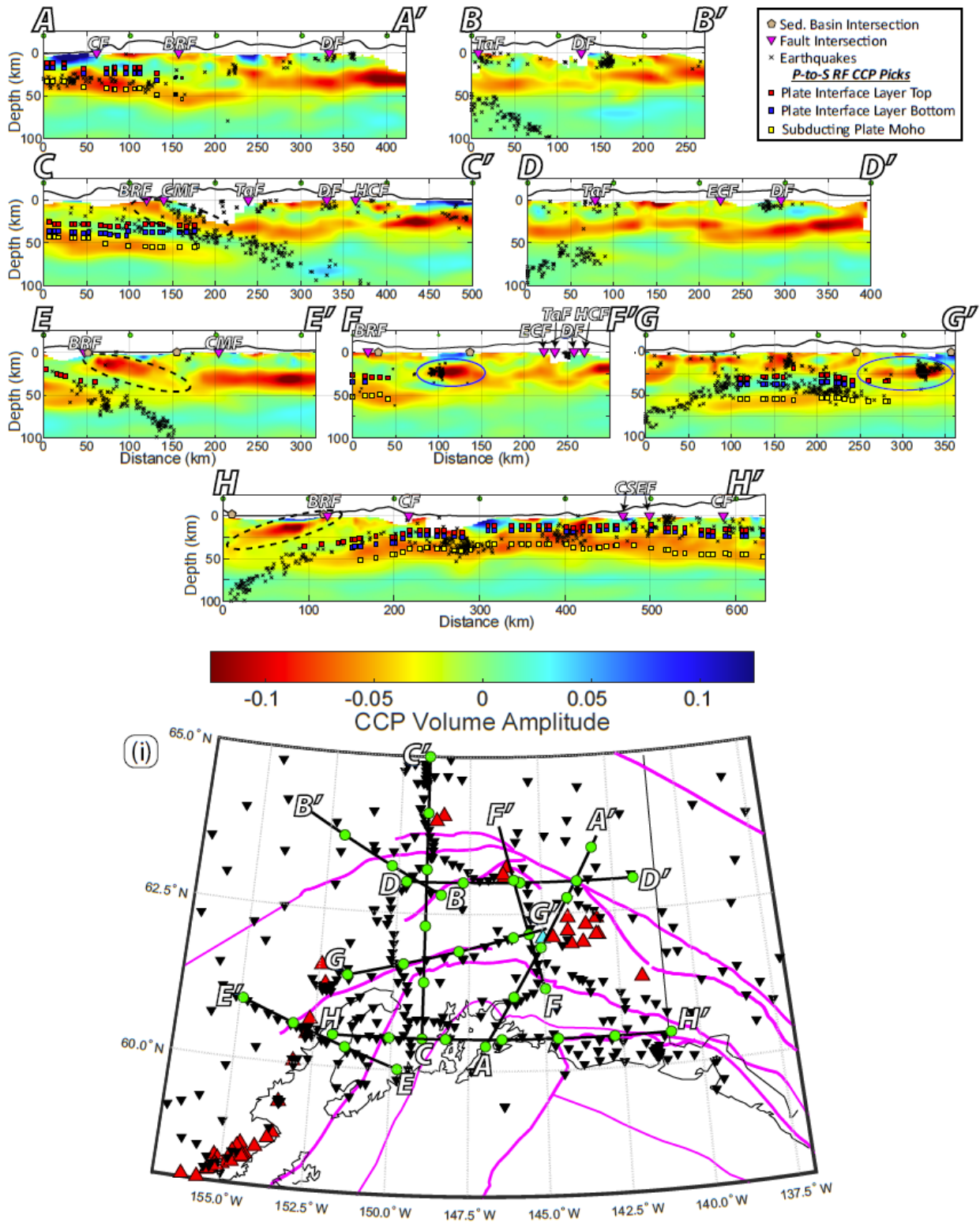


75

76 *Figure 1: Overview of study area. (a) Topographic map of study region showing volcanoes and two major sedimentary basins*
 77 *discussed in the text. CIB—Cook Inlet Basin. CRB—Copper River Basin. MRVF—Maclaren River Volcanic Field (Brueseke et al., 2023).*
 78 *Outline of Figure 5 is depicted with dashed black lines. (b) Terrane map of study region showing major faults. TiF—Tintina Fault,*
 79 *DF—Denali Fault, HCF—Hines Creek Fault, TaF—Talkeetna Fault, CMF—Castle Mountain Fault, BRF—Border Ranges Fault, CF—*
 80 *Contact Fault, CSEF—Chugach-St. Elias Fault, TrF—Transition Fault, ECF—Eureka Creek Fault. (c) Location of seismic stations used*
 81 *in this study. Outline of Yakutat oceanic plateau shown in shaded gray, with tear highlighted in dark red. Approximate*
 82 *delineation of three segments (i.e., western, central, and eastern) is shown. (d) Weighted ray coverage at 50-km depth in the Sp*
 83 *CCP volume. We only interpret along cross sections where the weighted ray coverage is greater than 0.4.*
 84

85 **2. Geologic Background**

86 The accretion of the Wrangellia composite terrane (WCT) to North American affinity
87 crust was the largest addition of crust to the continent in the last 200 million years (Trop and
88 Ridgway, 2007). The generally accepted model is that the WCT, primarily oceanic plateau crust
89 (Greene et al., 2010), collided along North America's western (east-dipping) subduction margin



91 Figure 2: Cross sections through the Sp CCP volume analyzed in this study. *Negative CCP stack amplitudes*
92 *correspond to positive velocity gradients (PVG) and positive stack amplitudes correspond to negative velocity gradients (NVG).*
93 *Each cross section is referenced as its own figure component, corresponding to the first letter of each line. For example, line A-A'*
94 *is "Figure 2a". Small red, blue, and yellow squares plotted on each cross section are from Mann et al. (2022) Ps RF CCP imaging*
95 *of the subducting Yakutat crust across the same region, using mostly the same seismometers. Small x's are earthquake*
96 *hypocenters within 5 km of the cross section. Hypocenter locations are from Daly et al. (2021) to the east of 149°W (where they*
97 *reported high-quality hypocenters), and from the Alaska Earthquake Center catalog to the west of 149°W. The locations where*
98 *major faults (Figure 1b) cross each cross section are marked with an inverted magenta triangle and label. The locations where*
99 *the lines cross the Copper River and Cook Inlet basins (Figure 1a) are in tan pentagons, plotted at z = 0 km. All fault labels (black*
100 *and white lettering) are from Figure 1b. Blue ovals highlight the PVG discussed in Section 5.2.4. Black dashed ovals highlight PVG*
101 *signal seen dipping inboard from the BRF. Green circles along cross sections denote locations along lines on map in part (i).*

102 at around ca. 100 Ma and then was translated >2000 km north along margin-parallel strike-slip
103 fault systems (e.g., Tikoff et al., 2023). The Alaska Range suture zone (Ridgway et al., 2002;
104 Trop et al., 2019) is the suture region between the WCT and rocks of North American affinity to
105 the north (Figure 1). The Denali Fault System (Amand, 1957) delineates the northern boundary
106 of the Alaska Range suture zone (Trop et al., 2019, 2020), and the Talkeetna Fault delineates the
107 southern boundary of the Alaska Range suture zone (Brennan et al., 2011).

108 By ca. 50 Ma, the Chugach-Prince William Terrane had been translated north and
109 accreted into place south of the BRF of southern Alaska (Figure 1) (Freeland & Dietz, 1973;
110 MacKevett & Plafker, 1974; Cowan, 2003; Garver and Davidson, 2015). The Contact Fault
111 delineates the suture between the Chugach and Prince William Terrane (Fisher & Magoon, 1978;
112 Nilsen & Zuffa, 1982). Both the BRF and Contact Fault were likely originally subduction
113 megathrusts which later experienced strike-slip motion (Plafker et al., 1989; Fuis et al., 1991;
114 Bol and Roeske, 1993; Brocher et al., 1994; Bruhn et al., 2004; Trop and Ridgway, 2007). The
115 BRF system has experienced at least ~700 km of slip between ca. 58 Ma and 50 Ma (Smart et al.,
116 1996) playing a role in the northward translation of the Chugach-Prince William Terrane,
117 whereas the Contact Fault experienced an undetermined amount of strike-slip motion during the
118 Eocene and during more recent times (e.g., Bol and Roeske, 1993; Chapman et al., 2012).

119 The most recent accretion event affecting southern Alaska involves the Yakutat
120 microplate which is a buoyant oceanic plateau with between 11-km (northern subducted leading
121 edge) and 30-km thick crust (south-east outboard segment) (e.g., Eberhart-Phillips et al., 2006;
122 Rondenay et al., 2008; Christeson et al., 2010; Worthington et al., 2012; Mann et al., 2022).
123 Crustal thickness also varies west (~17 km) to east (~30 km) (Figure 3) (Worthington et al.,
124 2012).

125 The Wrangell Arc is linked to the initiation of shallow-slab subduction of the Yakutat
126 oceanic plateau (ca. 30 Ma; Brueseke et al., 2019). The arrival of the Yakutat slab at Alaska's
127 southern convergent margin is also associated with deformation and mountain building across
128 much of southern Alaska (Abers, 2008; Enkelmann et al., 2010; Arkle et al., 2013; Benowitz et
129 al., 2019; Terhune et al., 2019).

130 The Neogene Yakutat "flat" slab subduction (Pavlis et al., 2004; Eberhart-Phillips et al.,
131 2006; Enkelmann et al., 2010) and true Yakutat collision (Gulick et al., 2007; Brueseke et al.,
132 2023) has also had a profound impact on the evolving structural configuration of the St. Elias
133 syntaxis region (eastern segment) (Figure 1c; e.g., Koons et al., 2010; Spotilia & Berger, 2010;
134 Jadamec et al., 2013; Enkelmann et al., 2015a). During the last ~3 Ma, faults with historically
135 primarily strike-slip kinematics experienced significant dip-slip motion (Berger et al., 2008;
136 Pavlis et al., 2012; Schartman et al., 2019). The St. Elias region deformation front may also have
137 shifted trenchward toward the south (Enkelmann et al., 2015a; Schartman et al., 2019).

138 The dynamic nature of the St. Elias syntaxis region has led to much debate on not only
139 which faults are active and reactivated through time in this region, but also the orientation-
140 kinematics of these structures (e.g., Bruhn et al. 2012). These concerns are compounded by some

141 authors referring to the far-eastern contact fault as the Contact fault (e.g., Bruhn et al., 2004),
142 others referring to the far-eastern contact fault as the Bagley fault (Bruhn et al., 2012), and still
143 others having the Bagley fault and Contact fault being different structures (Berger et al., 2008;
144 Chapman et al., 2012). Though beyond the spatial resolution of our results (estimated at ~10 km
145 laterally at Moho depths; e.g., Lekić et al., 2011) to resolve these <5-km scale mapping concerns,
146 we feel confident assuming that the Contact fault and the BRF are not back thrusts, because this
147 would imply these paleo-subduction interfaces have been overturned significantly.

148 **3. Data and Methods**

149 The southern Alaska subduction zone has seen the deployment of multiple dense (<~20-
150 km spacing) broadband seismometer arrays that cover most of the road system (Ferris et al.,
151 2003; Li et al., 2013; Bauer et al., 2014; Tape et al., 2017; Daly et al., 2021). These dense arrays,
152 supplemented with other permanent stations and smaller temporary arrays, provide excellent
153 station density across the shallow subduction zone and allow for imaging of continuous features
154 along-strike over hundreds of kilometers (e.g., Bauer et al., 2014; Kim et al., 2014). Recent P-to-
155 S RF (Ps RF) imaging across southern Alaska (Mann et al., 2022) has revealed the continuity and
156 subduction of the Yakutat oceanic plateau across the region, a thin low-velocity zone along the
157 plate interface atop the subducting Yakutat crust, and a North-South trending tear in the
158 subducting slab below ~50-km depth (Brueseke et al., 2023). This newly imaged tear (Mann et
159 al., 2022) has a broadly similar orientation, but a different location than the tear inferred by Fuis
160 et al. (2008).

161 In this study, teleseismic S-waves recorded on seismometers across southern Alaska
162 (Figure 1) were used to analyze the S-to-P scattered wavefield for crustal structure. Compared to

163 Ps RFs, there are several advantages to using Sp RFs for regional seismic imaging. First, the
164 conversion points are farther from the stations and can provide higher-fold imaging between
165 stations that are spaced too far apart for overlapping Ps RF Fresnel zones at upper-plate depths.
166 Second, Sp RFs contain one scattering mode (Figure 2), whereas Ps RFs record a superposition
167 of multiple scattering modes resulting from surface-reflected and back-scattered phases (e.g.,
168 Rondenay, 2009). Additionally, sedimentary basin multiples can obscure part of the record in Ps
169 RFs (e.g., Sheehan et al., 1995; Cunningham & Lekić, 2019), but large basin multiples arrive
170 after the S-wave arrival and therefore do not cause “ringing” in Sp RFs.

171 To generate the Sp common conversion point (CCP) volume, S-wave data were analyzed
172 following the procedure of Hua et al. (2020a). To improve vertical resolution of the Moho and
173 other crustal velocity gradients, waveform data were filtered with a 2 s to 30 s bandpass filter.
174 We chose this filter to highlight crustal structure, in contrast to the Sp CCP stacking of Gama et
175 al. (2022a), which employed a similar approach with a longer period bandpass (2 s to 100 s) in
176 order to optimize imaging of mantle structure. Particle motion analysis of the beginning of the P-
177 and S-waves on the P- and SV- components, respectively, was conducted to estimate “surface”
178 velocities at each station, and was used with a free-surface transform (Kennett, 1991) to isolate
179 the incident S wave from the converted P waves. All teleseismic S waves (Figures 1) recorded by
180 the stations between 06/01/1999 and 04/19/2020 were analyzed, and events that had SV-
181 components with signal-to-noise ratio > 1.5 , defined as the ratio of the average within a 5 s
182 signal window to that within a 25 s noise window, were used to generate Sp receiver functions
183 (RFs). The resulting Sp RFs were migrated to their common conversion points using a regional
184 3D shear-velocity (V_s) model (Feng & Ritzwoller, 2019) and a 3D compressive-wave velocity

185 (Vp) model generated from that 3D Vs model with shallow (<60 km) Vp/Vs constrained by
186 receiver function phase stacking (Mann et al., 2022). The Vp/Vs for all points below the phase
187 stacking depth were taken at each depth from the AK135 velocity model (e.g., Kennett et al.,
188 1995). The Sp RFs were stacked on a 3D grid of nodes (0.1° longitude x 0.1° latitude x 0.5 km in
189 depth). At a given depth, the weighting of individual RFs at each point was determined with a
190 horizontal Fresnel zone approximation based on 3D Sp RF isochrons plus geometrical spreading,
191 and assuming non-zero weights only within the area where the “isochron slope angle” was less
192 than 12° (see Hua et al., 2020a for full explanation).

193 Two other quality control parameters were used to cull the set of Sp RFs before stacking.
194 First, Sp RFs that did not have a prominent negative-amplitude (associated with a positive-
195 velocity gradient, PVG) Moho phase between 10-km and 60-km depth were excluded (following
196 Hua et al., 2020a). In Sp RFs, the most prominent phase is associated with the Moho, and even
197 though the upper plate Moho in subduction zones sometimes disappears or inverts in RF polarity
198 (e.g., Bostock et al., 2002), we found that this step considerably improved the clarity of observed
199 features in the CCP stack. Second, Sp RFs with anomalously high amplitudes in the mantle depth
200 range were removed. Mantle velocity gradients are not expected to exceed those typically
201 observed at the Moho (e.g., Krueger et al., 2021), so for times corresponding to the depth range
202 of 100-450 km, Sp RFs with root mean square values greater than 0.2 were eliminated. These
203 quality control steps resulted in 76,772 Sp RFs at the 734 stations, with an average of 105 per
204 station. We use stations across a wider region of southern Alaska for our analysis, but we do not
205 interpret results outside the regions of dense station spacing (Figure 1d, Figure 2). Following
206 Hua et al. (2020a), after stacking the Sp RFs at depth, interpretation of features was limited to the

207 region with higher sampling, i.e., where the weighted stack value (Figure 1d; equation 27 from
208 Hua et al., 2020a) is greater than 0.4.

209 Resolution for RF signals depends on frequency content and velocity along the scattered-
210 wave ray path (e.g., Rondenay, 2009). Assuming a minimum signal period of 2 s, Sp scattered-
211 phase wavelengths at Moho depths should be 8-9.8 km (at the crust-mantle interface depths, V_s
212 = 4.0-4.8 km/s), and vertical resolution for imaging subhorizontal discontinuities is therefore
213 approximately 4-4.8 km, assuming that vertical resolution from converted waves is
214 approximately half a wavelength (Bostock, 1999).

215 Dip resolution for Sp CCP stacking is more difficult to quantify because it depends on a
216 number of factors, including station spacing and distribution, the ray parameter and back-
217 azimuthal ranges of incident S-waves, signal-to-noise, and the presence of adjacent boundaries.
218 Overall, the shape of Sp RF sensitivity kernels yields better resolution of subhorizontal features
219 (e.g., Hansen & Schmandt, 2017; Hua et al., 2020). However, tests with synthetic data show that
220 shallow-dipping ($< \sim 15^\circ$) intracrustal boundaries have been imaged using Sp CCP stacking along
221 dense lines of stations (e.g., Hopper et al., 2017). At mantle depths, dip-resolution tests using
222 CCP stacking of synthetics indicate that dipping boundaries are resolvable up to dips of 10-15°
223 (Lekić & Fisher, 2017; Hua et al., 2020a). Even though this maximum resolvable dip (i.e., $\sim 15^\circ$)
224 may be an underestimate at crustal depths, we do not interpret features with apparent dips $> \sim 15^\circ$.

225 **4. Results**

226 The Sp CCP volume contains clear features that represent conversions from the Moho
227 and intracrustal interfaces. We categorize each velocity gradient interpreted here as a negative
228 velocity gradient (NVG; velocity decreasing with depth) or positive velocity gradient (PVG;

229 velocity increasing with depth) instead of using RF polarity or CCP amplitude. PVGs correspond
230 to negative Sp RF amplitudes (the convention used in the figures in this paper), although in some
231 other studies the sign of Sp amplitudes were flipped to match the association of PVGs with
232 positive Ps amplitudes.

233 The most prominent feature in the Sp CCP volume is a consistent PVG in the upper 20-
234 65 km depth range everywhere in the CCP volume. This PVG can be divided into two regions. In
235 the south where subduction is occurring, the PVG strikes roughly parallel to the trench and dips
236 inboard, and likely represents the Moho of the modern subducting slab. This interpretation is
237 supported by the continuity of the PVG with the dipping seismicity associated with the
238 subducting slab (Figure 2a,c,e,h). Across the remaining region, the PVG is subhorizontal
239 between 20-50 km depth with some sharp offsets in depth and corresponds with the upper-plate
240 Moho (Figure 2). In the southern subduction region, a NVG overlies and parallels the dipping
241 PVG at depths < 50 km nearly everywhere. This feature is likely the plate interface between
242 subducting and overriding crust.

243 Other imaged features exist within the upper-plate crust across the region. At the western
244 end, inboard-dipping PVGs extend from the surface to upper-plate Moho depths beneath the
245 Kenai Peninsula and the region just to the north of the Kenai Peninsula (Figure 2c,e,h). These
246 dipping PVGs intersect the surface at the trace of the BRF (Pavlis, 1982), but only exist along
247 the western segment of the BRF system (west of $\sim 149^\circ\text{W}$). Additionally, a strong subhorizontal
248 PVG is imaged at ~ 25 -km depth beneath the northern/northeastern portion of the Copper River
249 Basin (Figure 2f,g). This PVG extends for over 100-km East-West (between 147°W and 145°W)
250 and ~ 50 -km North-South (between 62°N and 62.5°N). At this PVG's southeastern corner, the

251 feature coincides with a dense cluster of earthquakes between 15-30 km depth (Figure 2f,g; Daly
252 et al., 2021) directly beneath the Klawasi group mud volcanoes (Figure 1) which have mantle
253 fluid isotopic signatures, are linked to an inferred deep-seated magmatic intrusive, and are
254 located ~20 km to the west of the main Wrangell Volcanic Arc (Figure 1; Motyka et al., 1989;
255 Brueseke et al., 2019).

256 **5. Discussion**

257 *5.1 The Subducting Yakutat Crust*

258 The subducting Yakutat Moho is imaged nearly everywhere as an inboard-dipping PVG
259 that agrees well with previous Ps RF imaging (Mann et al., 2022) (Figure 2a,c,e,f). Along line G-
260 G', which is roughly along-strike of the subducting Yakutat slab, the top and bottom of the
261 western half of the Yakutat crust are imaged at ~40- and ~60-km depth, respectively. This
262 provides further evidence that the Yakutat is subducting at a very shallow angle between 150°W
263 and 147.5°W (Figure 2g), and this result matches the Ps RF imaging across the region quite well
264 (e.g., Mann et al., 2022).

265 The plate interface is imaged as a NVG nearly everywhere atop the subducting Yakutat
266 plateau in the Sp CCP imaging and parallels the Yakutat Moho (Figure 2). This NVG is co-
267 located with a thin LVL imaged atop the subducting Yakutat crust across the region using
268 higher-resolution Ps RF phases (e.g., Kim et al., 2014; Mann et al., 2022). The Sp RF phases
269 used here have slightly less volumetric resolution than the upgoing P-to-S analog conversion
270 (“Pxs”), and significantly less resolution than surface-reflected, back-scattered RF phases. The
271 fact that the plate interface appears as a single NVG here with lower Sp RF resolution (c.f. Mann
272 et al., 2022) suggests that the top boundary of the LVL generates a converted wave with greater

273 amplitude than the bottom boundary of the LVL, and destructive interference between the two
274 converted waves results in a single apparent NVG. The top of the LVL being a stronger velocity
275 contrast is consistent with high resolution local earthquake scattering analysis (e.g., Kim et al.,
276 2019). Additionally, Ps RF migration images using only Pxs show a NVG across the top of the
277 subducting crust where the higher-resolution surface-reflected RF phases show a thin low-
278 velocity zone (e.g., Kim et al., 2014; Mann et al., 2022).

279 This single NVG along the plate interface resembles structures documented in subduction
280 zones with thinner subducting crust (<10 km; e.g., Audet et al., 2009; Abers et al., 2009) than the
281 Yakutat slab (11-30 km; Ferris et al., 2003; Rossi et al., 2006; Rondenay et al., 2008;
282 Worthington et al., 2012; Christeson et al., 2013; Kim et al., 2014; Mann et al., 2022), and raises
283 a long-debated question as to what this imaged feature represents. At these depths, the velocity
284 of the overriding crust should be lower than in the subducting basalt, so a NVG at the interface
285 between these two features is not expected without the presence of sediment and tectonically
286 eroded material along the interface (e.g., Abers et al., 2009; Kim et al., 2014; Mann et al., 2022)
287 or significant porosity and pore-fluids (e.g., Peacock et al., 2011). Additionally, high-resolution
288 seismic tomography models do not show a decrease in velocity across the interface, suggesting
289 that the cause of the NVG is either too thin or too sparse to image completely (e.g., Calvert et al.,
290 2020). Given the fact that Sp RFs have lower resolution than Ps RFs, and the subduction zone
291 structure in this region has been extensively studied using Ps RFs (e.g., Kim et al., 2014; Mann et
292 al., 2022), we only show the Ps RF CCP volume picks for the plate interface LVL and
293 subducting Moho for comparison and to reinforce the crustal imaging results discussed below.

294 ***5.2 Upper-Plate Crustal Structure***

295 We interpreted cross sections of the Sp CCP volume for crustal thickness and internal
296 structure along paths that follow dense station spacing across the region. These cross sections are
297 compared with the locations of other features, such as major faults, terrane boundaries, and
298 earthquakes (Figure 2).

299 ***5.2.1 Border Ranges Fault***

300 The BRF separates the inboard WCT from the seaward Chugach-Prince William Terrane
301 (Pavlis, 1982) and is one of the most identifiable topographic surface features across Southern
302 Alaska (Figure 3). The BRF began as a paleo-subduction zone plate interface that accommodated
303 northward subduction beneath the Wrangellia composite terrane from Early Jurassic to Late
304 Cretaceous time (e.g., Pavlis & Roeske, 2007; Trop & Ridgeway, 2007). Only scattered
305 remnants of this paleo-subduction interface are still identifiable at the surface. The BRF system
306 now consists of several branches that have juxtaposed different rock packages at different times
307 (Plafker et al., 1989).

308 An inboard-dipping PVG extends from the surface trace of the BRF to >25-km depths
309 across the northern and western sides of the Kenai Peninsula (Figure 2c,e,h). The North-South
310 line C-C' shows this feature dipping to the north at $\sim 15^\circ$ extending from the BRF at the surface
311 to the continental Moho (Figure 2c). Along lines E-E' and H-H', a similar feature dips to the
312 west at $\sim 15^\circ$ beneath the Cook Inlet Basin (Figure 2e,h). We considered three geologic features
313 that may be related to this PVG. (1) The PVG may be the top of accreted, high-velocity
314 ultramafic-mafic rocks of the Border Range ultramafic and mafic assemblages which lie along
315 the BRF system (e.g., Clark, 1973; Plafker et al., 1989; Kusky et al., 2007). (2) the PVG may be
316 a sliver of Border Range ultramafic and mafic assemblages at shallow depths followed by the

317 top of a subhorizontal serpentinized body in the lower crust seen at ~15 km depth beneath the
318 southeastern part of Cook Inlet Basin(Mankhemthong et al., 2013). (3) the PVG is a signal from
319 the base of the ~5-7-km thick Cook Inlet Basin (Shellenbaum et al., 2010).

320 If the inboard-dipping PVG is the top of a serpentinized body, then the serpentinization
321 could have resulted from fluid interaction within the overriding crust when the BRF was the
322 subduction interface. However, serpentinization decreases seismic velocities (e.g., Bostock et al.,
323 2002), so RF phases with the opposite polarity (i.e., NVG) may be expected, depending on the
324 degree of serpentinization (Hyndman & Peacock, 2003). While the inboard-dipping PVG does
325 not preclude serpentinization of the lowermost crust below the Kenai Peninsula and Cook Inlet
326 Basin (e.g., Mankhemthong et al., 2013), it is unlikely that such a strong PVG could result from
327 the top of a serpentinized body at these shallow crustal depths.

328 If the PVG is the base of the overlying Cook Inlet Basin, then this PVG is simply an
329 imaging artifact. However, the geometry of the PVG is inconsistent with this interpretation. Sp
330 RF phases are expected from the base of the overlying Cook Inlet Basin, but such arrivals would
331 likely be subhorizontal across much of the basin (Shellenbaum et al., 2010; Kim et al., 2014;
332 Smith & Tape, 2020). For example, the base of the ~5-7-km thick Cook Inlet Basin
333 (Shellenbaum et al., 2010) should create a subhorizontal PVG from $x = 0-120$ km on line H-H'.
334 However, the apparently subhorizontal part of the PVG only exists in the southeastern end of the
335 basin, even though a subhorizontal PVG segment is expected throughout the basin given that
336 there is more than sufficient station coverage (Figure 2e,h). The inboard-dipping PVG seems to
337 continue beneath the basin to depths > 25 km. Moreover, the PVG is seen both outside the

338 boundary of Cook Inlet Basin (line C-C') and within the basin (lines E-E' and H-H'). Therefore,
339 we do not think the dipping PVG is the result of artifacts from basin conversions.

340 We prefer the interpretation that the PVG feature is related to the inboard-dipping
341 Mesozoic paleo-subduction interface along the BRF system between the inboard WCT and
342 Border Range ultramafic and mafic assemblages (Clark, 1973; Kusky et al., 2007; Pavlis et al.,
343 2019), with the Cook Inlet Basin conversions superimposed over this PVG feature in the Sp CCP
344 volume along lines E-E' and H-H'. The next seaward terrane boundary, the Contact Fault (Figure
345 1b), has shallow, inboard-dipping structures beneath it as well (e.g., Fisher et al., 1983; Stephens
346 et al., 1990; Ye et al., 1997; Eberhart-Phillips et al., 2006) although they are too shallow and/or
347 small-scale to image with the Sp data in this study.

348 Both the BRF and Contact Fault were reactivated and experienced strike-slip motion
349 during the Paleocene-Eocene (Bol & Roeseke et al., 1993; Pavlis & Roeseke, 2007; Berger et al.,
350 2008). It has been documented that paleo-subduction interfaces can experience strike-slip motion
351 without reorganization or rotation towards vertical of deep structure (e.g., Sato et al., 2015).
352 However, the preservation of low-angle dip of the BRF paleo-subduction interface along the
353 western segment (i.e., Kenai Peninsula) may in part explain why major strike-slip Eocene
354 displacement (Garver and Davidson, 2015) was transferred onto other structures (Pavlis and
355 Roeseke, 2007). Strike-slip along the western BRF region may have been accommodated on the
356 nearby Eagle River Fault (Amato et al., 2013; Garver personal communication) and/or the Castle
357 Mountain Fault (Pavlis & Roeseke, 2007).

358 There are no apparent shallow-dipping features in this CCP volume to the east of
359 ~149°W, where the buoyant Yakutat oceanic plateau has been subducting since ca. 30 Ma (e.g.,

360 Brueseke et al., 2019). This could mean that the dip of the BRF has been rotated towards vertical
361 through extensive contraction and is now dipping too steeply to image with Sp CCP stacking
362 (e.g., Enkelmann et al., 2010; Arkle et al., 2013; Mankhemthong et al., 2013).

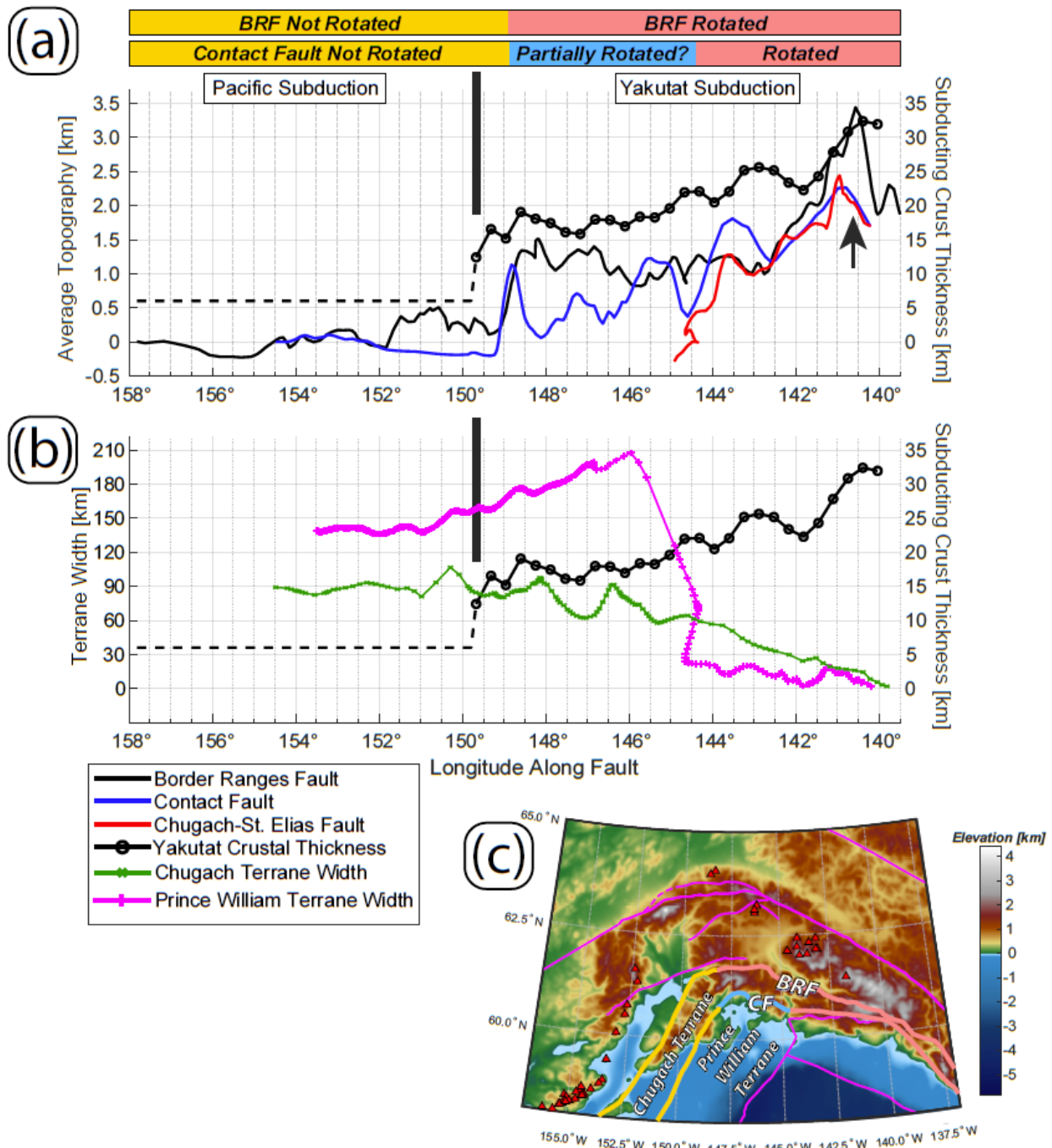
363 The BRF east of $\sim 149^\circ\text{W}$ may have been (partially?) rotated towards vertical during the
364 oblique transport and accretion of the Chugach and Prince William Terranes. Conversely, if
365 contraction related to buoyant Yakutat subduction is in part the reason for the absence of the
366 imaged BRF paleo-subduction interface, the Contact Fault paleo-subduction interface managed
367 to be preserved at least to 145.2°W with an inboard dip of $\sim 30^\circ$ under the central segment
368 (Figure 3), as seen in active-source seismic studies (e.g., Fuis et al., 1991). The lithological
369 similarities of the Chugach and Prince William Terranes (deep-water turbidites both sides of the
370 Contact Fault) may in part explain why west of 145.2°W the Contact Fault was not rotated
371 compared to the BRF (deep-water turbidites to the south, oceanic plateau-island arc to the north),
372 which has a greater across-strike change in crustal properties (Trop and Ridgway, 2007;
373 Mankhemthong et al., 2013).

374 To further investigate the relationships between upper-plate deformation and the inferred
375 along-strike variation in dips of the BRF and Contact Faults, we measured along-strike variations
376 in topography by averaging values within 5 km of each terrane-bounding fault near the
377 subduction zone (i.e., BRF, Contact Fault, and Chugach-St. Elias Fault) and also estimated the
378 strike-normal thickness of both the Chugach and Prince William terranes (Figure 1b). These
379 values were compared with subducting Yakutat crustal thickness beneath the margin (from Mann
380 et al., 2022; Figure 3). A sharp change in topography along the major faults at $\sim 149^\circ\text{W}$
381 corresponds with the point between Yakutat subduction to the east and Pacific plate subduction

382 to the west (Kim et al., 2014; Mann et al., 2022). Additionally, the width of both the Chugach
383 and Prince William terranes decrease to the east, with the Prince William terrane eventually
384 pinching off around the collisional zone at $\sim 141^\circ\text{W}$ (e.g., Chapman et al., 2012) where the
385 subducting Yakutat crustal thickness exceeds 25-30 km (Figure 3). The elevation and terrane
386 width trends indicate significant shortening and deformation across the eastern half of the region,
387 probably related to buoyant Yakutat crust subduction (e.g., Abers, 2008). The west to east
388 transition from low to high deformation at $\sim 149^\circ\text{W}$ is well correlated with the rotation of the
389 BRF to a steeper dip inferred from Sp CCP stacking and previous studies (Enkelmann et al.,
390 2010; Arkle et al., 2013; Mankemthong et al., 2013). As previously described, the similar
391 rotation toward vertical inferred for the Contact Fault (e.g., Fuis et al., 1991) occurs farther east,
392 perhaps indicating that the western limit of the most intense deformation in the more seaward
393 terranes is also offset to the east. This latter conclusion is broadly consistent with the along-strike
394 topographic gradients for the Contact and Chugach-St. Elias Faults (Figure 3).

395 Where the Pacific plate is subducting to the west of the imaged Yakutat plateau
396 (Rondenay et al., 2008; Worthington et al., 2012; Kim et al., 2014; Mann et al., 2022) (i.e., west
397 of $\sim 149^\circ\text{W}$), the long-term exhumation rate is ~ 0.1 mm/yr (Valentino et al., 2016), and there has
398 been a minimum of exhumation (< 2 -3 km) and inferred shortening since ca. 30 Ma. Arkle et al.
399 (2013) demonstrated, with applied thermochronology, that the Contact Fault is a structural
400 barrier along the central segment (Figure 1), with > 11 km of Oligocene-to-Present exhumation
401 north of the fault (exhumation rate of ~ 0.7 mm/yr) and just a few kilometers of exhumation
402 (exhumation rate of ~ 0.2 mm/yr) to the south during the same time frame. Hence, the Contact
403 Fault paleo-subduction interface may have played a role in focusing Oligocene-to-Present

404 deformation to the north in this region. Furthermore, in the central segment the BRF paleo-
405 subduction interface was rotated to a subvertical position and also facilitated vertical tectonics
406 (Figure 4). In this scenario the Maastrichtian(?) to Paleogene Contact Fault paleo-subduction
407 interface (Bol and Roeske, 1993; Brocher et al., 1994; Fuis & Plafker, 1991; Davidson & Garver,
408 2017) would be reactivated during the Oligocene-Neogene Yakutat shallow subduction event
409 (e.g., Arkle et al., 2013).



410

411 *Figure 3: Analysis of topography along the BRF and Contact Fault, and the intervening terranes' approximate thicknesses. It is*
 412 *inferred that the BRF is rotated to subvertical to the east of ~149°W, whereas the Contact Fault is rotated to subvertical to the*
 413 *east of ~145°W. (a) Comparison of subducting Yakutat thickness from Mann et al. (2022) with average topography within 5 km*
 414 *of each fault trace, plotted at the longitude of the fault. Arrow highlights the location of St. Elias syntaxis and collision*
 415 *(Enkelmann et al., 2010, 2015a, 2015b; Chapman et al., 2012) of thickest Yakutat terrane (Worthington et al., 2012; Mann et al.,*
 416 *2022; Brueseke et al., 2023). (b) Comparison of subducting Yakutat thickness with approximate widths of the Prince William and*
 417 *Chugach Terranes. (c) Peach color indicates portions of the Border Ranges and Contact faults that have been rotated to*

418 *subvertical. Unrotated sections are denoted by yellow lines. Potentially partially rotated section of Contact Fault is denoted by*
419 *blue line. These are also shown at top of figure plotted vs longitude. Shades of magenta colouring show offshore Yakutat crustal*
420 *thickness variations (Worthington et al., 2012).*

421 There is no seismic imaging of the geometry of the Contact Fault east of 145.2°W, but it
422 has been inferred that the fault was rotated towards vertical after ca. 5 Ma (Enkelmann et al.,
423 2008; Chapman et al., 2012). In this region, where both the BRF and Contact Faults have
424 inferred sub-vertical dips, exhumation rates in places are >5 mm/yr (Enkelmann et al., 2015b).
425 The west to east variability in BRF and Contact Faults structural geometry align with known
426 exhumation patterns (Arkle et al., 2013; Valentino et al., 2016; Enkleman et al., 2015b). Low-
427 angle structures are inefficient at exhumation and accommodate contraction more through
428 horizontal than vertical motion (e.g., Reiners and Brandon, 2006), whereas vertical structures
429 facilitate vertical extrusion of crustal blocks (e.g., Benowitz et al., 2022). Overall, the dramatic
430 along-strike variability in structural dip of the BRF and Contact faults implies three different
431 structural configurations operating along the same Oligocene-to-Present trench, aligning with
432 previous work that has highlighted margin-parallel variations in deformation history (Figure 4)
433 (Buscher et al., 2008; Enkelmann et al., 2010; Arkle et al., 2013; Valentino et al., 2016).

434 **5.2.2 Denali and Hines Creek Faults**

435 The upper-plate Moho typically shallows by 5-10 km northward across the Denali Fault
436 system in the profiles analyzed in this study (Figure 2a,b,c,f). The one exception is line D-D',
437 where a shallowing of the Moho across the Denali Fault is more gradual. Crustal thickness of the
438 Yukon-Tanana terrane, which is north of the Denali Fault, is only analyzed along lines of dense
439 station spacing to avoid artifacts due to sparse sampling of the CCP volume. The Moho offset
440 across the Denali Fault system has been imaged by fault-zone head-wave analysis (Allam et al.,
441 2017), RF migration (Allam et al., 2017; Miller et al., 2018; Mann et al., 2022), inversions of

442 surface-wave data (Haney et al., 2020), joint inversion of RFs and surface-wave data (e.g.,
443 Martin-Short et al., 2018; Gama et al., 2022b), and other imaging techniques (for a review, see
444 Yang et al., *this volume*). In the Hines Creek Fault region (Figure 1b), prior studies have found
445 that the crustal thickness step is larger across the Hines Creek Fault than the Denali Fault (e.g.,
446 Veenstra et al., 2006; Rossi et al., 2006; Allam et al., 2017; Miller et al., 2018). On the
447 comparable profile from the Sp CCP stack in the study (line C-C'; Figure 2c) the apparent Moho
448 offset actually lies somewhat closer to the Denali Fault than to the Hines Creek Fault, which at
449 this longitude lies ~20 km to the north. However, this difference may reflect the lower horizontal
450 resolution provided by Sp phases, relative to Ps data at a comparable period (e.g., Hansen &
451 Schmandt, 2017; Mancinelli & Fischer, 2017; Hua et al., 2020a; Hua et al., 2020b).

452 **5.2.3 Eureka Creek Fault**

453 The most prominent Moho depth offset imaged across the region in the Sp CCP volume
454 is a ~15-km eastward increase in crustal thickness on line D-D' (Figure 2d) where it crosses the
455 mapped surface trace of the Eureka Creek Fault (Nokleberg et al., 1985). There is also a ~10-km
456 northward increase in crustal thickness across the Eureka Creek Fault along line D-D'. These
457 crustal thickness offsets are very close to the location of newly discovered volcanoes and fissures
458 which lie above the western limb of the tear in the subducting Yakutat slab (Figure 1a) (Brueseke
459 et al., 2023).

460 The Eureka Creek Fault juxtaposes two significantly different subterranean of the WCT:
461 the Tangle subterranean to the south and the Slana River subterranean to the north (Nokleberg et al.,
462 1985). Not much had been known about the orientation of the Eureka Creek Fault at depth nor its
463 slip-history (e.g., Nokleberg et al., 1985; Nokleberg et al., 1989), but the apparent vertical offset

464 in Moho thickness across the fault is likely an inherited feature from when these two subterrane
465 were juxtaposed across an active strike-slip fault. Overall, the Eureka Creek Fault represents a
466 good example of an ancient subterrane-bounding fault maintaining crustal thickness offsets
467 through time.

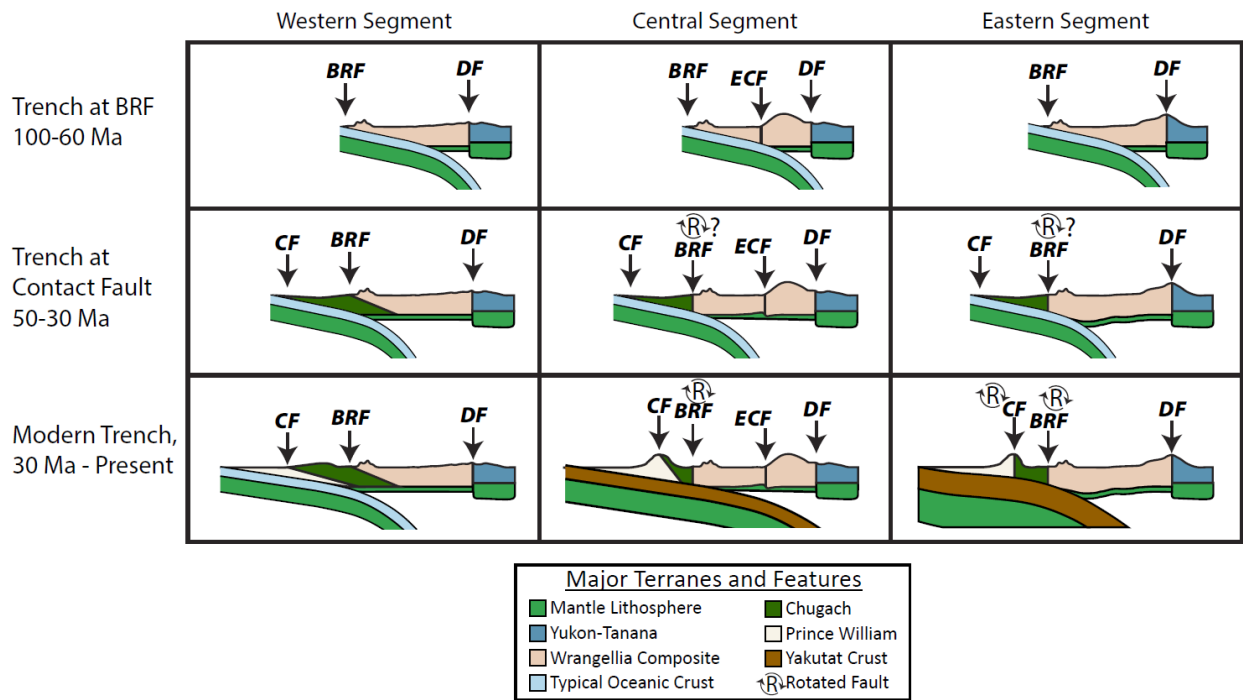
468 ***5.2.4 Crustal Structure Beneath Copper River Basin Region***

469 The PVG imaged at ~25-km depth beneath the Copper River Basin extends
470 approximately from 147°W to 145°W, and 62°N to 62.5°N (Figure 2f,g). The maximum
471 thickness of the basin reaches ~2 km (Fuis et al., 1991; Powell et al., 2019), which would result
472 in PVGs at depths <10-km, so this feature is not related to conversions at the base of the basin.
473 However, the PVG does extend throughout the basin and may indicate a link between these
474 features.

475 The mid-crustal PVG is directly above the ca. 1 Ma shallow tear in the subducting
476 Yakutat slab (Figure 5; Mann et al., 2022; Brueseke et al., 2023). A dense cluster of earthquake
477 hypocenters falls at the southeastern boundary of the PVG, near the Klawasi group mud
478 volcanoes (Figure 5; Daly et al., 2021). A NVG follows the PVG at 25-km depth in the
479 southeastern corner, which is especially pronounced beneath the cluster of earthquakes (Figure
480 2g), and finally beneath that is a weak PVG at ~50-km depth which matches the depth where
481 there is a velocity increase in both Ps RF imaging (Mann et al., 2022) and along the TACT lines
482 (e.g., Fuis et al., 1991).

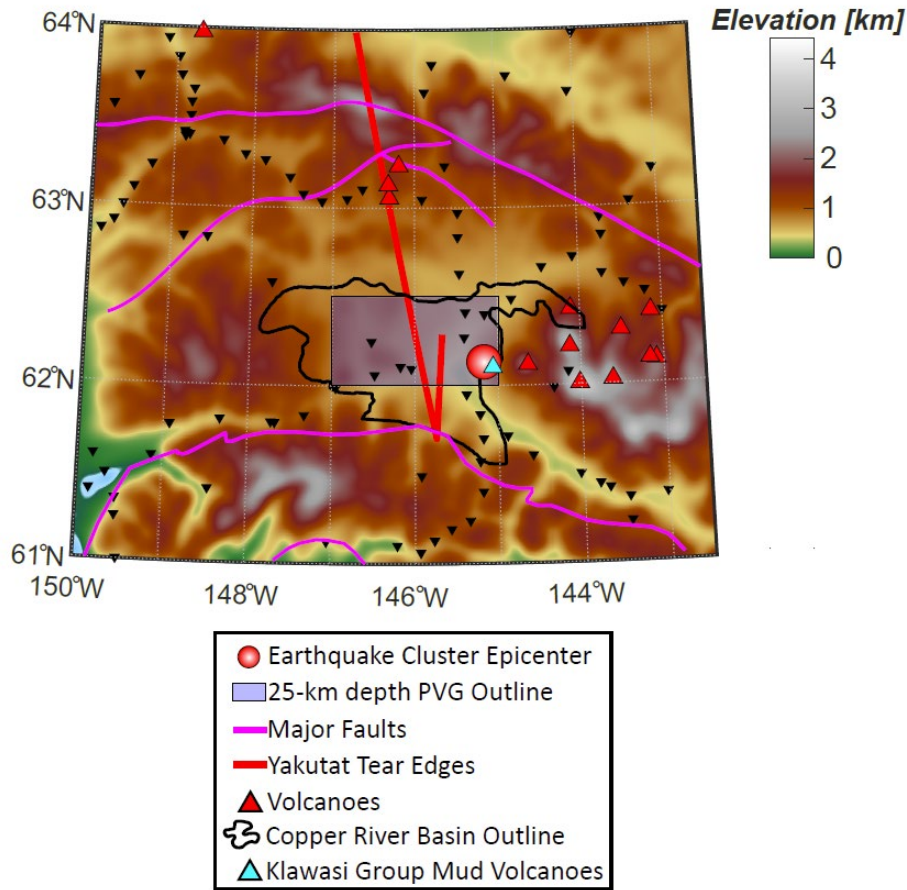
483 Other studies have also found anomalous structures beneath the Copper River Basin. The
484 North-South TACT line through the eastern part of the basin reported compressional velocities
485 of ~6.7-6.9 km/s (e.g., Fuis & Plafker, 1991) below ~20-km depth which more closely match that

486 of basalt and not continental crust (Brocher, 2005). Refracted P-waves from explosions in
 487 College Fjord at the northwest corner of Prince William Sound were recorded traveling at ~6.8
 488 km/s at stations along the Richardson Highway (paralleling line F-F', Figure 2f) but arrived ~1-
 489 second delayed along paths crossing this region (Hales & Asada, 1966). This delay was
 490 interpreted as resulting from anomalous lower crust and uppermost mantle velocities along these
 491 paths and is not the result of Moho depth variations. Additionally, the TACT line extending East-
 492 West through the Copper River Basin recorded no Pn or PmP throughout this region, further
 493 suggesting the lower crust and uppermost mantle beneath this region are anomalous (Goodwin et
 494 al., 1989).
 495



496
 497 *Figure 4: Schematic depicting snapshots through time of each of the three segments (Figure 1c) and whether or not the BRF*
 498 *and/or Contact Fault have been rotated toward subvertical. The central and eastern segments of BRF may have been rotated*
 499 *during ca 60- 50 Ma oblique translation and accretion of the Chugach and Prince William Terrane or this fault rotation from*
 500 *~15° toward sub-vertical may be related, at least in part, to the Yakutat oceanic plateau subduction. Whereas only the eastern*
 501 *segment of the Contact fault has been rotated from ~15° to ~30° towards subvertical where the Yakutat slab is the thickest*
 502 *(Figure 3). See text for further discussion and references. Note: thicknesses and dip angles in this figure are not drawn to scale.*

503 Based on the TACT active-source experiment results, the region from 20-50 km depth
504 beneath the Copper River Basin was interpreted as having formed from three possible scenarios:
505 (1) North-to-South tectonic underplating of lower North American crust beneath the Wrangellia
506 and Peninsular Terranes, (2) South-to-North tectonic underplating by the Kula plate, or (3)
507 magmatic underplating at some point since the late Cretaceous (Fuis & Plafker, 1991). Tectonic
508 underplating of lower North American crust from the north is not supported by the presence of
509 the sharp offset in crustal thickness across the Eureka Creek faults just to the north of this region
510 (see Section 4.2.3). Such a crustal thickness offset probably would have been obliterated if
511 buoyant lower crust was underthrust southward beneath the region. The subvertical lithospheric-
512 scale nature of the Denali-Hines Creek fault (Gama et al., 2022b; Newell et al., 2023) further
513 discounts scenario (1). Furthermore, the imaged inboard-dipping BRF Mesozoic paleo-
514 subduction interface supports a model of inboard-dipping (east and northward) subduction
515 polarity from the Mesozoic to the Present (Pavlis et al., 2019).



516

517 *Figure 5: Zoom in of the Copper River Basin and subducting Yakutat slab tear region (outline shown in Figure 1a), highlighting*
518 *the coincidence of (1) the earthquake cluster at ~25-km depth immediately to the west of the Wrangell Arc (Daly et al., 2021),*
519 *(2) the PVG seen at ~25-km depth beneath the Copper River Basin, and (3) underlying subducting slab tear location (Mann et al.,*
520 *2022).*

521

Between the two remaining possible scenarios, (2) and (3), we prefer the interpretation

522

that the source of the subhorizontal mid-crustal PVG is due to magmatic underplating and/or

523

intrusion. The location of this feature abutting against the western limb of the torn Yakutat slab

524

and directly above a nascent slab window (Figure 5; Mann et al., 2022; Brueseke et al., 2023),

525

next to the WVF and below Holocene mud volcanoes, and overlapping with a dense cluster of

526

earthquakes (Daly et al., 2021) suggests a connection between subducting slab tearing, crustal

527

structure, and volcano formation.

528 This scenario raises interesting questions about crustal thickness across the region. If the
529 sharp PVG at ~25-km depth beneath the Copper River Basin is the base of the Moho, then
530 ponding of basaltic melt into the thin (Gama et al., 2022a) mantle lithosphere of the upper plate
531 may explain the weak underlying PVG at ~50-km depth and the velocities seen in the TACT
532 experiment (Fuis et al., 1991). This scenario would imply that there is a ~20-25-km thick layer of
533 mantle containing ponded melt beneath the upper plate, directly above the tear in the subducting
534 slab. However, if the PVG at ~50-km depth (Figure 2g; Fuis et al., 1991; Ward & Lin, 2018) is
535 the upper plate Moho, then this would require a very large 20-25 km eastward increase in Moho
536 depth within the Copper River Basin to accommodate the shallow Yakutat slab imaged at ~30-
537 km depth on its western end (Figure 2). Maintaining such an abrupt crustal thickness offset over
538 a geologically significant amount of time would be especially challenging in the dynamically
539 active environment created by the subduction of Yakutat crust. Therefore, we prefer the
540 interpretation that the PVG at ~25-km depth is the upper-plate Moho beneath the Tangle
541 subterrane of the WCT (e.g., Nokleberg et al., 1985). This scenario would mean that the reduced
542 velocities in the mantle lithosphere and underlying mantle (i.e., between ~20-50 km depth) seen
543 in active-source results (Fuis et al., 1991), local explosion travel-time analysis (e.g., Hales &
544 Asada, 1966; Goodwin et al., 1989), and recent tomographic results from a joint inversion of RFs
545 and surface wave data (e.g., Ward & Lin, 2018) suggest significant underplating and intrusion of
546 basaltic magmatism into the upper plate, rising from the shallow tear in the subducting Yakutat
547 slab.

548 All of these features point toward significant alteration of the crust immediately to the
549 west of the Wrangell Volcanic Field and east of the shallow-dipping subducting Yakutat slab

550 (Figure 5), directly above the tear in the subducting Yakutat slab. A tear or window in a
551 subducting slab would allow for influx of hot asthenospheric mantle into the mantle wedge (e.g.,
552 Jadamec & Billen, 2012; Jadamec, 2016; Király et al., 2020) and may rapidly dehydrate and
553 eclogitize subducting crust, leading to significant alterations in the tectonics of the subducting
554 Yakutat slab (e.g., Brueseke et al., 2023), increase in mantle flow (e.g., Jadamec & Billen, 2010),
555 and partial melting rising to the surface which may pond beneath and/or intrude the upper-plate
556 crust. Given the cessation of the westward/northwestward younging age trend and magmatism of
557 the Wrangell Arc at ca. 1 Ma (Richter et al., 1990; Trop et al., 2022), we speculate that the
558 coincidence of the various geophysical observations directly beneath the Klawasi group mud
559 volcanoes just to the west of the youngest Wrangell Arc volcanos (e.g., Sanford, Drum,
560 Wrangell) (Figure 5; Trop et al., 2022) is evidence that these mud volcanos may be signs of
561 growth of the next generation Wrangell Volcanic Field tear volcano.

562 **6. Conclusions**

563 The relatively high-resolution Sp CCP imaging presented here provides one of the best
564 images of crustal architecture across the active Alaskan convergent margin that are free from the
565 effects of reverberations found in Ps RF studies and that sample more widely than active-source
566 studies. This kind of imaging is only possible due to decades of work deploying dense
567 seismometer arrays across the region, which allow for imaging and tracing of upper-plate crustal
568 architecture across the region.

569 Major findings include:

- 570 1) The plate interface is imaged as a NVG above the parallel subducting slab Moho across the
571 Yakutat slab shallow subduction region and agrees well with previous Ps RF imaging.

572 2) This southern Alaska Sp CCP imaging, combined with previous seismic imaging (e.g.,
573 Stephens et al., 1990; Fuis et al., 1991; Ye et al., 1997) and tectonic reconstructions (e.g., Trop
574 and Ridgway, 2007) provide insight into why low-angle paleo-subduction interfaces are
575 preserved in some locations, and rotated toward vertical with time in other places along the
576 margin. The western segment of the BRF preserves the inboard (paleo-east) dipping ($\sim 15^\circ$)
577 Mesozoic paleo-subduction interface to at least ~ 25 -km depth, but there the BRF may extend
578 further to the upper-plate Moho at ~ 35 -km depth. The next seaward terrane boundary, the
579 Contact Fault between the Chugach Terrane and the Prince William Sound Terrane, is also
580 imaged along the western segment as a shallow dipping ($\sim 15^\circ$) detachment (e.g., Stephens et al.,
581 1990; Ye et al., 1997). In the central transitional segment, the BRF subduction interface is
582 rotated toward vertical (Figure 2; e.g., Fuis et al., 1991) but the Contact Fault is not (dips $\sim 30^\circ$;
583 Fuis et al., 1991), whereas both the BRF and Contact Faults are rotated towards vertical along
584 the eastern segment (Figure 3; Enkelmann et al., 2008; Chapman et al., 2012). These seismic
585 observations in part reflect the differences in Oligocene-to-Present slab thickness between the
586 Pacific and Yakutat segments of the BRF and across-fault lithologic variations. To the east, both
587 the BRF and Contact Fault have been rotated towards vertical where the Yakutat plateau crust is
588 thickest (~ 25 to 30 km), and this contraction is evidenced by significant shorting across the
589 Prince William Terrane (Figure 3). In summary, Eocene soft-docking of the Chugach and Prince
590 William Terranes via strike-slip faulting (Garver and Davidson, 2015) limited Oligocene-to-
591 Present contraction, and ongoing Pacific slab subduction along the western segment (Buscher et
592 al., 2008; Valentino et al., 2016) has preserved the Mesozoic BRF and the Eocene-Oligocene
593 Contact Fault subduction interface.

594 3) Discrete upper-plate Moho offsets across terrane (Denali-Hines Creek faults) and sub-terrane
595 (Eureka Creek Fault) boundaries on the order of 10-km highlight significant Mesozoic crustal-
596 scale terrane tectonics. The imaged inboard-dipping BRF Mesozoic paleo-subduction interface
597 supports a model of inboard-dipping (east and northward) subduction polarity from the Mesozoic
598 to the Present (Pavlis et al., 2019), which is also consistent with the upper-plate Moho offsets.
599 4) We conclude that the newly imaged crust beneath the Copper River Basin, which likely has a
600 thickness of ~25 km, is underplated and significantly magmatically intruded and altered,
601 potentially due to excessive melt rising from the underlying slab tear and ponding beneath the
602 upper plate crust (Daly et al., 2021; Mann et al., 2022). These features and the overlying mud
603 volcanos with mantle fluid isotopic signatures (Motyka et al., 1989) indicate potential for the
604 creation of a new Yakutat slab tear volcano in the Wrangell Volcanic field.

605 In summary, by applying Sp RF imaging along dense lines of seismometers, we
606 document the preservation of Jura-Cretaceous terrane boundaries and a Mesozoic paleo-
607 subduction interface and the along-strike rotation toward vertical of the same paleo-subduction
608 interface due at least in part to Oligocene-to-Present buoyant Yakutat oceanic plateau
609 subduction. Along-strike variations in subduction zone indenter history and across-strike
610 lithological contrasts are common features of many long-lived convergent margins and the
611 results of this study may have bearing on how inherited crustal features affect later deformation
612 patterns globally.

613 **Acknowledgements**

614 We thank J. Hua for help in implementing the CCP stacking codes. The manuscript was
615 improved through the comments and suggestions of S. Gulick, G. Fuis, and two anonymous

616 reviewers and benefitted from the foundational work of the USGS Trans-Alaska Crustal Transect
617 (TACT) project. This work was supported by NSF EAR-2053042 and Woods Hole
618 Oceanographic Institution OBS Instrument Center Postdoctoral Scholarship (M. E. M.) and NSF
619 EAR-1829401(K. M. F.).

620

621 **Data Availability Statement**

622 All data used in this study were obtained from the IRIS Data Management Center
623 (<https://ds.iris.edu/ds/nodes/dmc/>). IRIS Data Services are funded through the Seismological
624 Facilities for the Advancement of Geoscience and EarthScope (SAGE) Proposal of the National
625 Science Foundation (NSF) under Cooperative Agreement EAR-1261681.

626

Figure Captions

627 **Figure 6:** Overview of study area. (a) Topographic map of study region showing volcanoes and
628 two major sedimentary basins discussed in the text. CIB–Cook Inlet Basin. CRB–Copper River
629 Basin. Outline of Figure 5 is depicted with dashed black lines. (b) Terrane map of study region
630 showing major faults. TiF–Tintina Fault, DF–Denali Fault, HCF–Hines Creek Fault, TaF–
631 Talkeetna Fault, CMF–Castle Mountain Fault, BRF–Border Ranges Fault, CF–Contact Fault,
632 CSEF–Chugach-St. Elias Fault, TrF–Transition Fault, ECF–Eureka Creek Fault. (c) Location of
633 seismic stations used in this study. Outline of Yakutat oceanic plateau shown in shaded gray,
634 with tear highlighted in dark red. Approximate delineation of three segments (i.e., western,
635 central, and eastern) is shown. (d) Weighted ray coverage at 50-km depth in the Sp CCP volume.
636 We only interpret along cross sections where this is greater than 0.4.

637 **Figure 7:** Cross sections through the Sp CCP volume analyzed in this study. Negative CCP stack
638 amplitudes correspond to positive velocity gradients (PVG) and positive stack amplitudes
639 correspond to negative velocity gradients (NVG). Each cross section is referenced as its own
640 figure part, corresponding to the first letter each line. For example, line A-A' is “Figure 2a”.
641 Small red, blue, and yellow squares plotted on each cross section are from Mann et al. (2022) Ps
642 RF CCP imaging of the subducting Yakutat crust across the same region, using mostly the same
643 seismometers. Small x's are earthquake hypocenters within 5 km of the cross section.
644 Hypocenter locations are from Daly et al. (2021) to the east of 149°W (where they reported high-
645 quality hypocenters), and from the Alaska Earthquake Center catalog to the west of 149°W. The
646 locations where major faults (Figure 1b) cross each cross section are marked with an inverted
647 magenta triangle and label. The locations where the lines cross the Copper River and Cook Inlet
648 basins (Figure 1a) are in tan pentagons, plotted at $z = 0$ km. All fault labels (black and white
649 lettering) are from Figure 1b. Blue ovals highlight the PVG discussed in Section 5.2.4. Black
650 dashed ovals highlight PVG signal seen dipping inboard from the BRF. Green circles along cross
651 sections denote locations along lines on map in part (i).

652 **Figure 3:** Analysis of topography along the BRF and Contact Fault, and the intervening terranes'
653 approximate thicknesses. It is inferred that the BRF is rotated to subvertical to the east of
654 $\sim 149^\circ\text{W}$, whereas the Contact Fault is rotated to subvertical to the east of $\sim 145^\circ\text{W}$. (a)
655 Comparison of subducting Yakutat thickness from Mann et al. (2022) with average topography
656 within 5 km of each fault trace, plotted at the longitude of the fault. Arrow highlights the location
657 of St. Elias syntaxis and collision (Enkelmann et al., 2010, 2015a, 2015b; Chapman et al., 2012)
658 of thickest Yakutat terrane (Worthington et al., 2012; Mann et al., 2022; Brueseke et al., 2023).
659 (b) Comparison of subducting Yakutat thickness with approximate widths of the Prince William
660 and Chugach Terranes. (c) Peach color indicates portions of the Border Ranges and Contact
661 faults that have been rotated to subvertical. Unrotated sections are denoted by yellow lines.
662 Potentially partially rotated section of Contact Fault is denoted by blue line. These are also
663 shown at top of figure plotted vs longitude.

664 **Figure 8:** Schematic depicting snapshots through time of each of the three segments (Figure 1c)
665 and whether or not the BRF and/or Contact Fault have been rotated toward subvertical. The
666 central and eastern segments of BRF may have been rotated during ca 60- 50 Ma oblique
667 translation and accretion of the Chugach and Prince William Terrane or this fault rotation from

668 ~15° toward sub-vertical may be related, at least in part, to the Yakutat oceanic plateau
669 subduction. Whereas only the eastern segment of the Contact fault has been rotated from ~15° to
670 ~30° towards subvertical where the Yakutat slab is the thickest (Figure 3). See text for further
671 discussion and references. Note: thicknesses and dip angles in this figure are not drawn to scale.

672 **Figure 5:** Zoom in of the Copper River Basin and subducting Yakutat slab tear region (outline
673 shown in Figure 1a), highlighting the coincidence of (1) the earthquake cluster at ~25-km depth
674 immediately to the west of the Wrangell Arc (Daly et al., 2021), (2) the PVG seen at ~25-km
675 depth beneath the Copper River Basin, and (3) underlying subducting slab tear location (Mann et
676 al., 2022).

677

678

679 **References:**

- 680 Abers, G. A. (2008). Orogenesis from subducting thick crust and evidence from Alaska, in
681 *Active tectonics and seismic potential of Alaska, geophysical monograph series*. In J. T.
682 Freymueller, et al. (Eds.), (Vol. 179, pp. 337–349). AGU.
683 <https://doi.org/10.1029/179GM19>
- 684 Abers, G. A., MacKenzie, L. S., Rondenay, S., Zhang, Z., Wech, A. G., & Creager, K. C. (2009).
685 Imaging the source region of Cascadia tremor and intermediate-depth earthquakes.
686 *Geology*, 37(12), 1119–1122. <https://doi.org/10.1130/G30143A.1>
- 687 Allam, A. A., Schulte-Pelkum, V., Ben-Zion, Y., Tape, C., Ruppert, N., & Ross, Z. E. (2017).
688 Ten kilometer vertical Moho offset and shallow velocity contrast along the Denali fault
689 zone from double-difference tomography, receiver functions, and fault zone head waves.
690 *Tectonophysics*, 721, 56–69. <https://doi.org/10.1016/j.tecto.2017.09.003>
- 691 Alvarado, A., Audin, L., Nocquet, J. M., Jaillard, E., Mothes, P., Jarrín, P., et al. (2016).
692 Partitioning of oblique convergence in the Northern Andes subduction zone: Migration
693 history and the present-day boundary of the North Andean Sliver in Ecuador. *Tectonics*,
694 35(5), 1048–1065. <https://doi.org/10.1002/2016TC004117>
- 695 Amand, P.S. (1957). Geological and geophysical synthesis of the tectonics of portions of British
696 Columbia, the Yukon Territory, and Alaska. *Geological Society of America Bulletin*,
697 68(10), pp.1343-1370.
- 698 Amato, J.M., Pavlis, T.L., Clift, P.D., Kochelek, E.J., Hecker, J.P., Worthman, C.M., & Day,
699 E.M. (2013). Architecture of the Chugach accretionary complex as revealed by detrital
700 zircon ages and lithologic variations: Evidence for Mesozoic subduction erosion in south-
701 central Alaska. *Bulletin*, 125(11-12), pp.1891-1911.
- 702 Arkle, J.C., Armstrong, P.A., Haeussler, P.J., Prior, M.G., Hartman, S., Sendziak, K.L., & Brush,
703 J.A. (2013). Focused exhumation in the syntaxis of the western Chugach Mountains and
704 Prince William Sound, Alaska. *Bulletin*, 125(5-6), pp.776-793.
- 705 Audet, P., Bostock, M. G., Christensen, N. I., & Peacock, S. M. (2009). Seismic evidence for
706 overpressured subducted oceanic crust and megathrust fault sealing. *Nature*, 457(7225),
707 76–78. <https://doi.org/10.1038/nature07650>
- 708 Bauer, M. A., Pavlis, G. L., & Landes, M. (2014). Subduction geometry of the Yakutat terrane,
709 southeastern Alaska. *Geosphere*, 10(6), 1161–1176. <https://doi.org/10.1130/GES00852.1>
- 710 Benowitz, J.A., Roeske, S.M., Regan, S.P., Waldien, T.S., Elliott, J.L., & O’Sullivan, P.B.
711 (2022). Large-scale, crustal-block vertical extrusion between the Hines Creek and Denali
712 faults coeval with slip localization on the Denali fault since ca. 45 Ma, Hayes Range,
713 Alaska, USA. *Geosphere*, 18(3), pp.1030-1054.
- 714 Benowitz, J.A., Davis, K., & Roeske, S. (2019). A river runs through it both ways across time:
715 ⁴⁰Ar/³⁹Ar detrital and bedrock muscovite geochronology constraints on the Neogene

- 716 paleodrainage history of the Nenana River system, Alaska Range. *Geosphere*, 15(3),
717 pp.682-701.
- 718 Berger, A.L., Spotila, J.A., Chapman, J.B., Pavlis, T.L., Enkelmann, E., Ruppert, N.A., &
719 Buscher, J.T. (2008). Architecture, kinematics, and exhumation of a convergent orogenic
720 wedge: A thermochronological investigation of tectonic–climatic interactions within the
721 central St. Elias orogen, Alaska. *Earth and Planetary Science Letters*, 270(1-2), pp.13-24.
- 722 Blakely, R. J., Brocher, T. M., & Wells, R. E. (2005). Subduction-zone magnetic anomalies and
723 implications for hydrated forearc mantle. *Geology*, 33(6), 445.
724 <https://doi.org/10.1130/G21447.1>
- 725 Bostock, M. G., Hyndman, R. D., Rondenay, S., & Peacock, S. M. (2002). An inverted
726 continental Moho and serpentinization of the forearc mantle. *Nature*, 417(6888), 536–
727 538. <https://doi.org/10.1038/417536a>
- 728 Bol, A.J., & Roeske, S.M. (1993). Strike-slip faulting and block rotation along the contact fault
729 system, eastern Prince William Sound, Alaska. *Tectonics*, 12(1), pp.49-62.
- 730 Brennan, P., Gilbert, H., Ridgway, K. D. (2011), Crustal structure across the central Alaska
731 Range: Anatomy of a Mesozoic collisional zone, *Geochemistry Geophysics Geosystems*,
732 12(4).
- 733 Brocher, T.M., Fuis, G.S., Fisher, M.A., Plafker, G., Moses, M.J., Taber, J.J., & Christensen, N.I.
734 (1994). Mapping the megathrust beneath the northern Gulf of Alaska using wide-angle
735 seismic data. *Journal of Geophysical Research: Solid Earth*, 99(B6), pp.11663-11685.
- 736 Brocher, T. M. (2005). Empirical Relations between Elastic Wavespeeds, & Density in the
737 Earth’s Crust. *Bulletin of the Seismological Society of America*, 95(6), 2081–2092.
738 <https://doi.org/10.1785/0120050077>
- 739 Brueseke, M. E., Benowitz, J. A., Bearden, A. T., Mann, M. E., & Miggins, D. P. (2023).
740 Subduction disruption, slab tears: ca. 1 Ma true collision of an ~30-km-thick oceanic
741 plateau segment recorded by Yakutat slab nascent tear magmatism. *Terra Nova*, 35, 49–
742 57. <https://doi.org/10.1111/ter.12628>
- 743 Brueseke, M.E., Benowitz, J.A., Trop, J.M., Davis, K.N., Berkelhammer, S.E., Layer, P.W., &
744 Morter, B.K. (2019). The Alaska Wrangell Arc: ~30 Ma of subduction-related
745 magmatism along a still active arc-transform junction. *Terra Nova*, 31(1), pp.59-66.
- 746 Bruhn, R.L., Pavlis, T.L., Plafker, G., & Serpa, L. (2004). Deformation during terrane accretion
747 in the Saint Elias orogen, Alaska. *Geological Society of America Bulletin*, 116(7-8),
748 pp.771-787.
- 749 Bruhn, R.L., Sauber, J., Cotton, M.M., Pavlis, T.L., Burgess, E., Ruppert, N., & Forster, R.R.
750 (2012). Plate margin deformation and active tectonics along the northern edge of the
751 Yakutat Terrane in the Saint Elias Orogen, Alaska, and Yukon, Canada. *Geosphere*, 8(6),
752 pp.1384-1407.

- 753 Bruns, T. R. (1983). Model for the origin of the Yakutat block, an accreting terrane in the
754 northern Gulf of Alaska. *Geology*, *11*(12), 718. [https://doi.org/10.1130/0091-](https://doi.org/10.1130/0091-7613(1983)11<718:MFTOOT>2.0.CO;2)
755 [7613\(1983\)11<718:MFTOOT>2.0.CO;2](https://doi.org/10.1130/0091-7613(1983)11<718:MFTOOT>2.0.CO;2)
- 756 Buscher, J.T., Berger, A.L., & Spotila, J.A. (2008). Exhumation in the Chugach-Kenai Mountain
757 belt above the Aleutian subduction zone, southern Alaska. *Washington DC American*
758 *Geophysical Union Geophysical Monograph Series*, *179*, pp.151-166.
- 759 Calvert, A. J., Bostock, M. G., Savard, G., & Unsworth, M. J. (2020). Cascadia low frequency
760 earthquakes at the base of an overpressured subduction shear zone. *Nature*
761 *Communications*, *11*(1), 3874. <https://doi.org/10.1038/s41467-020-17609-3>
- 762 Chapman, J.B., Pavlis, T.L., Bruhn, R.L., Worthington, L.L., Gulick, S.P., & Berger, A.L.
763 (2012). Structural relationships in the eastern syntaxis of the St. Elias orogen, Alaska.
764 *Geosphere*, *8*(1), pp.105-126.
- 765 Christeson, G.L., Gulick, S.P., van Avendonk, H.J., Worthington, L.L., Reece, R.S., & Pavlis,
766 T.L. (2010). The Yakutat terrane: Dramatic change in crustal thickness across the
767 Transition fault, Alaska. *Geology*, *38*(10), pp.895-898..
- 768 Christeson, G.L., Van Avendonk, H.J.A., Gulick, S.P.S., Reece, R.S., Pavlis, G.L., & Pavlis,
769 T.L. (2013). Moho interface beneath Yakutat terrane, southern Alaska. *Journal of*
770 *Geophysical Research: Solid Earth*, *118*(9), pp.5084-5097.
- 771 Clark, S.H.B. (1973). The McHugh Complex of south-central Alaska. U.S. Geological Survey
772 Bulletin 1372-D, D1–D11.
- 773 Cowan, D.S. (2003). Revisiting the Baranof–Leech River hypothesis for early Tertiary coastwise
774 transport of the Chugach–Prince William terrane. *Earth and Planetary Science Letters*,
775 *213*(3-4), pp.463-475.
- 776 Cunningham, E., & Lekić, V. (2019). Constraining crustal structure in the presence of sediment:
777 a multiple converted wave approach. *Geophysical Journal International*, *219*(1), 313–
778 327. <https://doi.org/10.1093/gji/ggz298>
- 779 Daly, K. A., Abers, G. A., Mann, M. E., Roecker, S., & Christensen, D. H. (2021). Subduction of
780 an Oceanic Plateau Across Southcentral Alaska: High-Resolution Seismicity. *Journal of*
781 *Geophysical Research: Solid Earth*, *126*(11).
782 <https://doi.org/10.1029/2021JB022809> Davidson, C., & Garver, J.I., 2017. Age and origin
783 of the resurrection ophiolite and associated turbidites of the Chugach–Prince William
784 Terrane, Kenai Peninsula, Alaska. *The Journal of Geology*, *125*(6), pp.681-700.
- 785 Eberhart-Phillips, D., Christensen, D.J., Brocher, T.M., Hansen, R., Ruppert, N.A., Haeussler,
786 P.J., & Abers, G.A. (2006). Imaging the transition from Aleutian subduction to Yakutat
787 collision in central Alaska, with local earthquakes and active source data: *Journal of*
788 *Geophysical Research*, v. 111, B11303, doi: 10.1029/2005JB004240.
- 789 Enkelmann, E., Garver, J.I., & Pavlis, T.L. (2008). Rapid exhumation of ice-covered rocks of the
790 Chugach–St. Elias orogen, Southeast Alaska. *Geology*, *36*(12), pp.915-918.

- 791 Enkelmann, E., Zeitler, P.K., Garver, J.I., Pavlis, T.L., & Hooks, B.P. (2010). The
792 thermochronological record of tectonic and surface process interaction at the Yakutat–
793 North American collision zone in southeast Alaska. *American Journal of Science*, 310(4),
794 pp.231-260.
- 795 Enkelmann, E., Koons, P.O., Pavlis, T.L., Hallet, B., Barker, A., Elliott, J., Garver, J.I., Gulick,
796 S.P., Headley, R.M., Pavlis, G.L., & Ridgway, K.D. (2015a). Cooperation among
797 tectonic and surface processes in the St. Elias Range, Earth's highest coastal mountains.
798 *Geophysical Research Letters*, 42(14), pp.5838-5846.
- 799 Enkelmann, E., Valla, P.G., & Champagnac, J.D. (2015b). Low-temperature thermochronology
800 of the Yakutat plate corner, St. Elias Range (Alaska): Bridging short-term and long-term
801 deformation. *Quaternary Science Reviews*, 113, pp.23-38.
- 802 Feng, L., & Ritzwoller, M. H. (2019). A 3-D Shear Velocity Model of the Crust and Uppermost
803 Mantle Beneath Alaska Including Apparent Radial Anisotropy. *Journal of Geophysical
804 Research: Solid Earth*, 124(10), 10468–10497. <https://doi.org/10.1029/2019JB018122>
- 805 Ferris, A., Abers, G. A., Christensen, D. H., & Veenstra, E. (2003). High resolution image of the
806 subducted Pacific (?) plate beneath central Alaska, 50–150 km depth. *Earth and
807 Planetary Science Letters*, 214(3–4), 575–588. [https://doi.org/10.1016/S0012-
808 821X\(03\)00403-5](https://doi.org/10.1016/S0012-821X(03)00403-5)
- 809 Fisher, M.A. & Magoon, L.B. (1978). Geologic framework of lower Cook inlet, Alaska. *AAPG
810 Bulletin*, 62(3), pp.373-402.
- 811 Fisher, M. A., von Huene, R., Smith, G. L., & Bruns, T. R. (1983). Possible seismic reflections
812 from the downgoing Pacific Plate, 275 kilometers arcward from the Eastern Aleutian
813 Trench. *Journal of Geophysical Research: Solid Earth*, 88(B7), 5835–5849.
814 <https://doi.org/10.1029/JB088iB07p05835>
- 815 Freeland, G.L. & Dietz, R.S. (1973). Rotation history of Alaskan tectonic blocks.
816 *Tectonophysics*, 18(3-4), pp.379-389.
- 817 Fuis, G. S. & Plafker, G. (1991). Evolution of deep structure along the Trans-Alaska Crustal
818 Transect, Chugach Mountains and Copper River Basin, southern Alaska. *Journal of
819 Geophysical Research: Solid Earth*, 96(B3), 4229–4253.
820 <https://doi.org/10.1029/90JB02276>
- 821 Fuis, G. S., Ambos, E. L., Mooney, W. D., Christensen, N. I., & Geist, E. (1991). Crustal
822 structure of accreted terranes in southern Alaska, Chugach Mountains and Copper River
823 Basin, from seismic refraction results. *Journal of Geophysical Research: Solid Earth*,
824 96(B3), 4187–4227. <https://doi.org/10.1029/90JB02316>
- 825 Fuis, G. S., Moore, T. E., Plafker, G., Brocher, T. M., Fisher, M. A., Mooney, W. D., et al.
826 (2008). Trans-Alaska Crustal Transect and continental evolution involving subduction
827 underplating and synchronous foreland thrusting. *Geology*, 36(3), 267.
828 <https://doi.org/10.1130/G24257A.1>

- 829 Gama, I., Fischer, K. M., & Hua, J. (2022a). Mapping the Lithosphere and Asthenosphere
830 Beneath Alaska With Sp Converted Waves. *Geochemistry, Geophysics, Geosystems*,
831 23(10). <https://doi.org/10.1029/2022GC010517>
- 832 Gama, I., Fischer, K. M., Dalton, C. A., & Eilon, Z. (2022b). Variations in Lithospheric
833 Thickness Across the Denali Fault and in Northern Alaska. *Geophysical Research*
834 *Letters*, 49(24). <https://doi.org/10.1029/2022GL101256>
- 835 Garver, J.I. & Davidson, C.M. (2015). Southwestern Laurentian zircons in upper Cretaceous
836 flysch of the Chugach-Prince William terrane in Alaska. *American Journal of Science*,
837 315(6), pp.537-556.
- 838 Goodwin, E. B., Fuis, G. S., Nokleberg, W. J., & Ambos, E. L. (1989). The crustal structure of
839 the Wrangellia Terrane along the East Glenn Highway, eastern-southern Alaska. *Journal*
840 *of Geophysical Research: Solid Earth*, 94(B11), 16037–16057.
841 <https://doi.org/10.1029/JB094iB11p16037>
- 842 Greene, A.R., Scoates, J.S., Weis, D., Katvala, E.C., Israel, S., & Nixon, G.T. (2010). The
843 architecture of oceanic plateaus revealed by the volcanic stratigraphy of the accreted
844 Wrangellia oceanic plateau. *Geosphere*, 6(1), pp.47-73.
- 845 Gulick, S.P., Lowe, L.A., Pavlis, T.L., Gardner, J.V., & Mayer, L.A. (2007). Geophysical
846 insights into the Transition fault debate: Propagating strike slip in response to stalling
847 Yakutat block subduction in the Gulf of Alaska. *Geology*, 35(8), pp.763-766.
- 848 Hales, A. L., & Asada, T. (1966). Crustal Structure in Coastal Alaska. In J. S. Steinhart & T. J.
849 Smith (Eds.), *Geophysical Monograph Series* (pp. 420–432). Washington, D. C.:
850 American Geophysical Union. <https://doi.org/10.1029/GM010p0420>
- 851 Haney, M. M., Ward, K. M., Tsai, V. C., & Schmandt, B. (2020). Bulk Structure of the Crust and
852 Upper Mantle beneath Alaska from an Approximate Rayleigh-Wave Dispersion Formula.
853 *Seismological Research Letters*, 91(6), 3064–3075. <https://doi.org/10.1785/0220200162>
- 854 Hansen, S. M. & Schmandt, B. (2017). P and S wave receiver function imaging of subduction
855 with scattering kernels. *Geochemistry, Geophysics, Geosystems*, 18(12), 4487-4502.
- 856 Hawkesworth, C., Cawood, P. A., & Dhuime, B. (2019). Rates of generation and growth of the
857 continental crust. *Geoscience Frontiers*, 10(1), 165–173.
858 <https://doi.org/10.1016/j.gsf.2018.02.004>
- 859 Hopper, E., Fischer, K. M., Wagner, L. S., & Hawman, R. B. (2017). Reconstructing the end of
860 the Appalachian orogeny. *Geology*, 45(1), 15–18. <https://doi.org/10.1130/G38453.1>
- 861 Hua, J., Fischer, K. M., Wu, M., & Blom, N. A. (2020a). New Approaches to Multifrequency Sp
862 Stacking Tested in the Anatolian Region. *Journal of Geophysical Research: Solid Earth*,
863 125(11). <https://doi.org/10.1029/2020JB020313>

- 864 Hua, J., Fischer, K. M., Mancinelli, N. J., & Bao, T. (2020b). Imaging with pre-stack migration
865 based on Sp scattering kernels, *Geophys. J. Int.*, 220, 428-449,
866 <https://doi.org/10.1093/gji/ggz459>
- 867 Hyndman, R. D., & Peacock, S. M. (2003). Serpentinization of the forearc mantle. *Earth and*
868 *Planetary Science Letters*, 212(3–4), 417–432. [https://doi.org/10.1016/S0012-](https://doi.org/10.1016/S0012-821X(03)00263-2)
869 [821X\(03\)00263-2](https://doi.org/10.1016/S0012-821X(03)00263-2)
- 870 Jadamec, M. A., & Billen, M. I. (2010). Reconciling surface plate motions with rapid three-
871 dimensional mantle flow around a slab edge. *Nature*, 465(7296), 338–341.
872 <https://doi.org/10.1038/nature09053>
- 873 Jadamec, M.A. & Billen, M.I., 2012. The role of rheology and slab shape on rapid mantle flow:
874 Three-dimensional numerical models of the Alaska slab edge. *Journal of Geophysical*
875 *Research: Solid Earth*, 117(B2).
- 876 Jadamec, M.A., Billen, M.I., & Roeske, S.M., 2013. Three-dimensional numerical models of flat
877 slab subduction and the Denali fault driving deformation in south-central Alaska. *Earth*
878 *and Planetary Science Letters*, 376, pp.29-42.
- 879 Jadamec, M.A., 2016. Insights on slab-driven mantle flow from advances in three-dimensional
880 modelling. *Journal of Geodynamics*, 100, pp.51-70.
- 881 Kawakatsu, H., Kumar, P., Takei, Y., Shinohara, M., Kanazawa, T., Araki, E., & Suyehiro, K.
882 (2009). Seismic evidence for sharp lithosphere-asthenosphere boundaries of oceanic
883 plates. *Science*, 324(5926), 499-502.
- 884 Kennett, B. L. N. (1991). The Removal of Free Surface Interactions From Three-Component
885 Seismograms. *Geophysical Journal International*, 104(1), 153–154.
886 <https://doi.org/10.1111/j.1365-246X.1991.tb02501.x>
- 887 Kennett, B. L. N., Engdahl, E. R., & Buland, R. (1995). Constraints on seismic velocities in the
888 Earth from traveltimes. *Geophysical Journal International*, 122(1), 108–124.
889 <https://doi.org/10.1111/j.1365-246X.1995.tb03540.x>
- 890 Kim, D., Keranen, K. M., Abers, G. A., & Brown, L. D. (2019). Enhanced Resolution of the
891 Subducting Plate Interface in Central Alaska From Autocorrelation of Local Earthquake
892 Coda. *Journal of Geophysical Research: Solid Earth*, 124(2), 1583–1600.
893 <https://doi.org/10.1029/2018JB016167>
- 894 Kim, Y., Abers, G. A., Li, J., Christensen, D., Calkins, J., & Rondenay, S. (2014). Alaska
895 Megathrust 2: Imaging the megathrust zone and Yakutat/Pacific plate interface in the
896 Alaska subduction zone. *Journal of Geophysical Research: Solid Earth*, 119(3), 1924–
897 1941. <https://doi.org/10.1002/2013JB010581>
- 898 Király, A., Portner, D.E., Haynie, K.L., Chilson-Parks, B.H., Ghosh, T., Jadamec, M.,
899 Makushkina, A., Manga, M., Moresi, L., & O'Farrell, K.A., (2020). The effect of slab
900 gaps on subduction dynamics and mantle upwelling. *Tectonophysics*, 785, p.228458.

- 901 Koons, P.O., Hooks, B.P., Pavlis, T., Upton, P., & Barker, A.D., (2010). Three-dimensional
902 mechanics of Yakutat convergence in the southern Alaskan plate corner. *Tectonics*, 29(4).
- 903 Korja, A., & Heikkinen, P. J. (2008). Seismic images of Paleoproterozoic microplate boundaries
904 in the Fennoscandian Shield. In *Special Paper 440: When Did Plate Tectonics Begin on*
905 *Planet Earth?* (Vol. 440, pp. 229–248). Geological Society of America.
906 [https://doi.org/10.1130/2008.2440\(11\)](https://doi.org/10.1130/2008.2440(11))
- 907 Krueger, H. E., Gama, I., & Fischer, K. M. (2021). Global Patterns in Cratonic Mid-Lithospheric
908 Discontinuities From Sp Receiver Functions. *Geochemistry, Geophysics, Geosystems*,
909 22(6). <https://doi.org/10.1029/2021GC009819>
- 910 Kumar, P., & Kawakatsu, H. (2011). Imaging the seismic lithosphere-asthenosphere boundary of
911 the oceanic plate: OCEANIC LAB IMAGING. *Geochemistry, Geophysics, Geosystems*,
912 12(1), n/a-n/a. <https://doi.org/10.1029/2010GC003358>
- 913 Kusky, T.M., Glass, A., & Bradley, D.C. (2007). Structure, Cr-chemistry, and age of the Border
914 Ranges ultramafic/mafic complex: A suprasubductionzone ophiolite complex. In:
915 Ridgway, K.D., Trop, J., Glen, M., & O'Neill, J.M. (eds) *Tectonic Growth of a*
916 *Collisional Continental Margin: Crustal Evolution of Southern Alaska*. Geological
917 Society of America, Special Papers, 431, 207–225.
- 918 Langston, C. A. (1977). Corvallis, Oregon, crustal and upper mantle receiver structure from
919 teleseismic *P* and *S* waves. *Bulletin of the Seismological Society of America*, 67(3), 713–
920 724. <https://doi.org/10.1785/BSSA0670030713>
- 921 Lekić, V., French, S. W., & Fischer, K. M. (2011). Lithospheric Thinning Beneath Rifted
922 Regions of Southern California. *Science*, 334(6057), 783–787.
923 <https://doi.org/10.1126/science.1208898>
- 924 Lekić, V. & Fischer, K. M. (2017). Interpreting spatially stacked Sp receiver
925 functions. *Geophysical Journal International*, 210(2), 874–886
- 926 Li, J., Abers, G. A., Kim, Y., & Christensen, D. (2013). Alaska megathrust 1: Seismicity 43
927 years after the great 1964 Alaska megathrust earthquake. *Journal of Geophysical*
928 *Research: Solid Earth*, 118(9), 4861–4871. <https://doi.org/10.1002/jgrb.50358>
- 929 Li, C., Gao, H., & Williams, M. L. (2020). Seismic characteristics of the eastern North American
930 crust with Ps converted waves: Terrane accretion and modification of continental crust.
931 *Journal of Geophysical Research: Solid Earth*, 125, e2019JB018727.
932 <https://doi.org/10.1029/2019JB018727>
- 933 Little, T. A., & Naeser, C. W. (1989). Tertiary tectonics of the Border Ranges Fault System,
934 Chugach Mountains, Alaska: Deformation and uplift in a forearc setting. *Journal of*
935 *Geophysical Research: Solid Earth*, 94(B4), 4333–4359.
936 <https://doi.org/10.1029/JB094iB04p04333>

- 937 Long, M. D., Benoit, M. H., Aragon, J. C., & King, S. D. (2019). Seismic imaging of mid-crustal
938 structure beneath central and eastern North America: Possibly the elusive Grenville
939 deformation? *Geology*, 47(4), 371-374.
- 940 MacKevett, E.M. & Plafker, G. (1974). The Border Ranges fault in south-central Alaska. *US*
941 *Geological Survey Journal of Research*, 2, pp.323-329.
- 942 Mancinelli, N. J. & Fischer, K. M. (2017). The spatial sensitivity of Sp converted waves---
943 Scattered wave kernels and their applications to receiver-function migration and
944 inversion, *Geophys. J. Int.*, 212, 1722–1735, <https://doi.org/10.1093/gji/ggx506>
- 945 Mankhemthong, N., Doser, D. I., & Pavlis, T. L. (2013). Interpretation of gravity and magnetic
946 data and development of two-dimensional cross-sectional models for the Border Ranges
947 fault system, south-central Alaska. *Geosphere*, 9(2), 242–259.
948 <https://doi.org/10.1130/GES00833.1>
- 949 Mann, M. E., Abers, G. A., Daly, K. A., & Christensen, D. H. (2022). Subduction of an Oceanic
950 Plateau Across Southcentral Alaska: Scattered-Wave Imaging. *Journal of Geophysical*
951 *Research: Solid Earth*, 127(1). <https://doi.org/10.1029/2021JB022697>
- 952 Margirier, A., Strecker, M. R., Reiners, P. W., Thomson, S. N., Casado, I., George, S. W. M., &
953 Alvarado, A. (2023). Late Miocene Exhumation of the Western Cordillera, Ecuador,
954 Driven by Increased Coupling Between the Subducting Carnegie Ridge and the South
955 American Continent. *Tectonics*, 42(1). <https://doi.org/10.1029/2022TC007344>
- 956 Martin-Short, R., Allen, R., Bastow, I. D., Porritt, R. W., & Miller, M. S. (2018). Seismic
957 Imaging of the Alaska Subduction Zone: Implications for Slab Geometry and Volcanism.
958 *Geochemistry, Geophysics, Geosystems*, 19(11), 4541–4560.
959 <https://doi.org/10.1029/2018GC007962>
- 960 Miller, M. S., O’Driscoll, L. J., Porritt, R. W., & Roeske, S. M. (2018). Multiscale crustal
961 architecture of Alaska inferred from P receiver functions. *Lithosphere*, 10, 267-278. 1050
962 doi: 10.1130/L701.1.
- 963 Motyka, R.J., Poreda, R.J., & Jeffrey, A.W. (1989). Geochemistry, isotopic composition, and
964 origin of fluids emanating from mud volcanoes in the Copper River basin, Alaska.
965 *Geochimica et Cosmochimica Acta*, 53(1), pp.29-41.
- 966 Newell, D.L, Benowitz, J.A., Regen, S.P., Hiatt, C.D., (2023). Roadblocks and speed limits:
967 Mantle-to-surface volatile flux through the lithospheric-scale Denali fault, Alaska:
968 *Geology*, v. 51, p. 576–580, <https://doi.org/10.1130/G51068.1>
- 969 Nilsen, T.H. & Zuffa, G.G. (1982). The Chugach terrane, a Cretaceous trench-fill deposit,
970 southern Alaska. *Geological Society, London, Special Publications*, 10(1), pp.213-227.
- 971 Nokleberg, W. J., Jones, D. L., & Silberling, N. J. (1985). Origin and tectonic evolution of the
972 Maclaren and Wrangellia terranes, eastern Alaska Range, Alaska. *Geological Society of*
973 *America Bulletin*, 96(10), 1251. [https://doi.org/10.1130/0016-](https://doi.org/10.1130/0016-7606(1985)96<1251:OATEOT>2.0.CO;2)
974 [7606\(1985\)96<1251:OATEOT>2.0.CO;2](https://doi.org/10.1130/0016-7606(1985)96<1251:OATEOT>2.0.CO;2)

- 975 Nokleberg, W. J., Foster, H. L., & Aleinikoff, J. N. (1989). Geology of the northern Copper
976 River basin, eastern Alaska range, and southern Yukon-Tanana Upland. In W. J.
977 Nokleberg & M. A. Fisher (Eds.), *Alaskan Geological and Geophysical Transect* (pp.
978 34–63). Washington, D. C.: American Geophysical Union.
979 <https://doi.org/10.1029/FT104p0034>
- 980 Pavlis, T.L. (1982). Origin and age of the Border Ranges fault of southern Alaska and its bearing
981 on the late Mesozoic tectonic evolution of Alaska. *Tectonics*, 1(4), pp.343-368.
- 982 Pavlis, T.L., Picornell, C., Serpa, L., Bruhn, R.L., & Plafker, G. (2004). Tectonic processes
983 during oblique collision: Insights from the St. Elias orogen, northern North American
984 Cordillera. *Tectonics*, 23(3).
- 985 Pavlis, T. L., & Roeske, S. M. (2007). The Border Ranges fault system, southern Alaska. In
986 *Special Paper 431: Tectonic Growth of a Collisional Continental Margin: Crustal*
987 *Evolution of Southern Alaska* (Vol. 431, pp. 95–127). Geological Society of America.
988 [https://doi.org/10.1130/2007.2431\(05\)](https://doi.org/10.1130/2007.2431(05))
- 989 Pavlis T.L., Chapman JB, Bruhn R.L., Ridgway K, Worthington LL, Gulick S.P., & Spotila J.
990 (2012). Structure of the actively deforming fold-thrust belt of the St. Elias orogen with
991 implications for glacial exhumation and three-dimensional tectonic processes. *Geosphere*.
992 2012 Oct 1;8(5):991-1019.
- 993 Pavlis, T.L., Amato, J.M., Trop, J.M., Ridgway, K.D., Roeske, S.M., & Gehrels, G.E. (2019).
994 Subduction polarity in ancient arcs: A call to integrate geology and geophysics to
995 decipher the Mesozoic tectonic history of the northern Cordillera of North America: *GSA*
996 *Today*, no. 11, v. 29, <https://doi.org/10.1130/GSATG402A.1>
- 997 Peacock, S. M., Christensen, N. I., Bostock, M. G., & Audet, P. (2011). High pore pressures and
998 porosity at 35 km depth in the Cascadia subduction zone. *Geology*, 39(5), 471–474.
999 <https://doi.org/10.1130/G31649.1>
- 1000 Plafker, G., Nokleberg, W. J., Lull, J. S. (1989). Bedrock geology and tectonic evolution of the
1001 Wrangellia, Peninsular, and Chugach Terranes along the Trans-Alaska Crustal Transect
1002 in the Chugach Mountains and Southern Copper River Basin, Alaska. *Journal of*
1003 *Geophysical Research: Solid Earth*, 94(B4), 4255-4295.
- 1004 Plafker, G. & Berg, H. C. (1994). Overview of the geology and tectonic evolution of Alaska. *The*
1005 *Geology of North America, GSA, Chapter 33*, 989-1021.
- 1006 Powell, Doug, & Amoco Oil Co. (2019), Geological report to the Ahtna Corporation, Copper
1007 River basin, Alaska, 1975: Alaska Division of Geological & Geophysical Surveys
1008 Geologic Materials Center Data Report 455, 26 p., 9 sheets.
1009 <https://doi.org/10.14509/30324>
- 1010 Reiners, P.W. & Brandon, M.T. (2006). Using thermochronology to understand orogenic
1011 erosion. *Annu. Rev. Earth Planet. Sci.*, 34, pp.419-466.

- 1012 Richter, D.H., Smith, J.G., Lanphere, M.A., Dalrymple, G.B., Reed, B.L., & Shew, N. (1990).
1013 Age and progression of volcanism, Wrangell volcanic field, Alaska. *Bulletin of*
1014 *Volcanology*, 53, pp.29-44.
- 1015 Ridgway, K.D., Trop, J.M., Nokleberg, W.J., Davidson, C.M., & Eastham, K.R. (2002).
1016 Mesozoic and Cenozoic tectonics of the eastern and central Alaska Range: Progressive
1017 basin development and deformation in a suture zone. *Geological Society of America*
1018 *Bulletin*, 114(12), pp.1480-1504.
- 1019 Rondenay, S. (2009). Upper mantle imaging with array recordings of converted and scattered
1020 teleseismic waves. *Surveys in Geophysics*, 30(4-5), 377-405.
1021 <https://doi.org/10.1007/s10712-009-9071-5>
- 1022 Rondenay, S., Abers, G. A., & van Keken, P. E. (2008). Seismic imaging of subduction zone
1023 metamorphism. *Geology*, 36(4), 275. <https://doi.org/10.1130/G24112A.1>
- 1024 Rossi, G., Abers, G. A., Rondenay, S., & Christensen, D. H. (2006). Unusual mantle Poisson's
1025 ratio, subduction, and crustal structure in central Alaska. *Journal of Geophysical*
1026 *Research*, 111(B9), B09311. <https://doi.org/10.1029/2005JB003956>
- 1027 Saltus, R. W., & Hudson, T. L. (2022). There is more Wrangellia — magnetic characterization of
1028 southern Alaska crust. *Canadian Journal of Earth Sciences*, 59(4), 243-257.
1029 <https://doi.org/10.1139/cjes-2020-0209>
- 1030 Sato, H., Kato, N., Abe, S., Van Horne, A., & Takeda, T. (2015). Reactivation of an old plate
1031 interface as a strike-slip fault in a slip-partitioned system: Median Tectonic Line, SW
1032 Japan. *Tectonophysics*, 644-645, 58-67. <https://doi.org/10.1016/j.tecto.2014.12.020>
- 1033 Schartman, A., Enkelmann, E., Garver, J.I., & Davidson, C.M. (2019). Uplift and exhumation
1034 of the Russell Fiord and Boundary blocks along the northern Fairweather transform fault,
1035 Alaska. *Lithosphere*, 11(2), pp.232-251.
- 1036 Sheehan, A. F., Abers, G. A., Jones, C. H., & Lerner-Lam, A. L. (1995). Crustal thickness
1037 variations across the Colorado Rocky Mountains from teleseismic receiver functions.
1038 *Journal of Geophysical Research: Solid Earth*, 100(B10), 20391-20404.
1039 <https://doi.org/10.1029/95JB01966>
- 1040 Shellenbaum, D. P., L. S. Gregersen,, & P. R. Delaney (2010). Top Mesozoic unconformity
1041 depth map of the Cook Inlet basin, Alaska, *Rept. Investig. 2010-2*, Alaska Division of
1042 Geological and Geophysical Surveys, Fairbanks, Alaska.
- 1043 Smart, K.J., Pavlis, T.L., Sisson, V.B., Roeske, S.M., & Snee, L.W., (1996), The Border Ranges
1044 fault system in Glacier Bay National Park, Alaska: evidence for major early Cenozoic
1045 dextral strike-slip motion, *Canadian Journal of Earth Sciences*, 33(9), pp.1268-1282.
- 1046 Smith, K., & Tape, C. (2020). Seismic Response of Cook Inlet Sedimentary Basin, Southern
1047 Alaska. *Seismological Research Letters*, 91(1), 33-55.
1048 <https://doi.org/10.1785/0220190205>

- 1049 Spotila, J.A. & Berger, A.L. (2010). Exhumation at orogenic indenter corners under long-term
1050 glacial conditions: Example of the St. Elias orogen, Southern Alaska. *Tectonophysics*,
1051 490(3-4), pp.241-256.
- 1052 Stephens, C. D., Page, R. A., & Lahr, J. C. (1990). Reflected and mode-converted seismic waves
1053 within the shallow Aleutian Subduction Zone, Southern Kenai Peninsula, Alaska. *Journal*
1054 *of Geophysical Research*, 95(B5), 6883. <https://doi.org/10.1029/JB095iB05p06883>
- 1055 Tape, C., Christensen, D., Moore-Driskell, M. M., Sweet, J., & Smith, K. (2017). Southern
1056 Alaska Lithosphere and Mantle Observation Network (SALMON): A Seismic
1057 Experiment Covering the Active Arc by Road, Boat, Plane, and Helicopter.
1058 *Seismological Research Letters*, 88(4), 1185–1202. <https://doi.org/10.1785/0220160229>
- 1059 Terhune, P.J., Benowitz, J.A., Trop, J.M., O’Sullivan, P.B., Gillis, R.J., & Freymueller, J.T.,
1060 (2019), Cenozoic tectono-thermal history of the southern Talkeetna Mountains, Alaska:
1061 Insights into a potentially alternating convergent and transform plate margin, *Geosphere*,
1062 15(5), pp.1539-1576.
- 1063 Tikoff, B., Housen, B. A., Maxson, J. A., Nelson, E. M., Trevino, S., & Shipley, T. F. (2023).
1064 Hit-and-run model for Cretaceous–Paleogene tectonism along the western margin of
1065 Laurentia. In S. J. Whitmeyer, M. L. Williams, D. A. Kellett, & B. Tikoff, *Laurentia:
1066 Turning Points in the Evolution of a Continent* (pp. 659–705). Geological Society of
1067 America. [https://doi.org/10.1130/2022.1220\(32\)](https://doi.org/10.1130/2022.1220(32))
- 1068 Trop, J.M., Benowitz, J.A., Kirby, C.S., & Brueseke, M.E. (2022). Geochronology of the
1069 Wrangell Arc: Spatial-temporal evolution of slab-edge magmatism along a flat-slab,
1070 subduction-transform transition, Alaska-Yukon. *Geosphere*, 18(1), pp.19-48.
- 1071 Trop, J.M., Benowitz, J.A., Koeppe, D.Q., Sunderlin, D., Brueseke, M.E., Layer, P.W., &
1072 Fitzgerald, P.G., (2020). Stitch in the ditch: Nutzotin Mountains (Alaska) fluvial strata
1073 and a dike record ca. 117–114 Ma accretion of Wrangellia with western North America
1074 and initiation of the Totschunda fault. *Geosphere*, 16(1), pp.82-110.
- 1075 Trop, J. M., Benowitz, J., Cole, R. B., & O’Sullivan, P. (2019), Cretaceous to Miocene
1076 magmatism, sedimentation, and exhumation within the Alaska Range suture zone: A
1077 polyphase reactivated terrane boundary, *Geosphere*, 15(4), pp.1066-1101.
- 1078 Trop, J. M., & Ridgway, K. D. (2007). Mesozoic and Cenozoic tectonic growth of southern
1079 Alaska: A sedimentary basin perspective. In *Special Paper 431: Tectonic Growth of a
1080 Collisional Continental Margin: Crustal Evolution of Southern Alaska* (Vol. 431, pp. 55–
1081 94). Geological Society of America. [https://doi.org/10.1130/2007.2431\(04\)](https://doi.org/10.1130/2007.2431(04))
- 1082 Valentino, J. D., Spotila, J. A., Owen, L. A., & Buscher, J. T. (2016). Rock uplift at the transition
1083 from flat-slab to normal subduction: The Kenai Mountains, Southeast Alaska.
1084 *Tectonophysics*, 671, 63–75. <https://doi.org/10.1016/j.tecto.2016.01.022>
- 1085 Veenstra, E., Christensen, D. H., Abers, G. A., & Ferris, A. (2006). Crustal thickness variation in
1086 south-central Alaska. *Geology*, 34(9), 781. <https://doi.org/10.1130/G22615.1>

- 1087 Ward, K. M., & Lin, F. (2018). Lithospheric Structure Across the Alaskan Cordillera From the
1088 Joint Inversion of Surface Waves and Receiver Functions. *Journal of Geophysical*
1089 *Research: Solid Earth*, 123(10), 8780–8797. <https://doi.org/10.1029/2018JB015967>
- 1090 Westerweel, J., Roperch, P., Licht, A., Dupont-Nivet, G., Win, Z., Poblete, F., et al. (2019).
1091 Burma Terrane part of the Trans-Tethyan arc during collision with India according to
1092 palaeomagnetic data. *Nature Geoscience*, 12(10), 863–868.
1093 <https://doi.org/10.1038/s41561-019-0443-2>
- 1094 Worthington, L.L., Van Avendonk, H.J., Gulick, S.P., Christeson, G.L., & Pavlis, T.L., 2012.
1095 Crustal structure of the Yakutat terrane and the evolution of subduction and collision in
1096 southern Alaska. *Journal of Geophysical Research: Solid Earth*, 117(B1).
- 1097 Ye, S., Flueh, E. R., Klaeschen, D., & Huene, R. (1997). Crustal structure along the EDGE
1098 transect beneath the Kodiak shelf off Alaska derived from OBH seismic refraction data.
1099 *Geophysical Journal International*, 130(2), 283–302. [https://doi.org/10.1111/j.1365-](https://doi.org/10.1111/j.1365-246X.1997.tb05648.x)
1100 [246X.1997.tb05648.x](https://doi.org/10.1111/j.1365-246X.1997.tb05648.x)
- 1101 Zhang, Y., Li, A., & Hu, H. (2019). Crustal structure in Alaska from receiver function analysis.
1102 *Geophysical Research Letters*, 46, 1284–1292. <https://doi.org/10.1029/2018GL081011>
- 1103
- 1104